This is the peer-reviewed, final accepted version for American Mineralogist, published by the Mineralogical Society of America.
The published version is subject to change. Cite as Authors (Year) Title. American Mineralogist, in press.
DOI: https://doi.org/10.2138/am-2024-9316. http://www.minsocam.org/

Word Count: 9372

Revision 2

Al^{3+} and H^{+} substitutions in TiO_2 polymorphs: structural and vibrational investigations

Sha Wang[1], Qingbo Wang[2], Yu Ye[1]*, Dan Liu[1,3], Xi Zhu[1], Yancheng Hu[1], Yunfan Miao[1], Zhen Wu[1], Yanming Pan[1]

[1]State Key Laboratory of Geological Processes and Mineral Resources, China University of Geosciences, Wuhan, 430074, China

[2]School of Mathematics and Physics, China University of Geosciences, Wuhan, 430074, China

[3]Gemmological Institute, China University of Geosciences, Wuhan, 430074, China

*Corresponding author: Yu Ye (yeyu@cug.edu.cn)

Abstract: Rutile is the most common TiO_2 mineral on Earth's surface and transforms to $CaCl_2$- and α-PbO_2-type structures at elevated pressures in subducted basaltic crusts. In this study, we synthesized hydrous $CaCl_2$- and α-PbO_2-TiO_2 crystals with various Al^{3+} concentrations using a multi-anvil press. Al^{3+} is incorporated into the $CaCl_2$- and

rutile-type phases mainly in the form of $3Ti^{4+} = 4Al^{3+}$, while the coupled substitution of $Ti^{4+} = Al^{3+} + H^{+}$ is dominant in the α-PbO_2-type structure, forming $Ti_{1-x}(AlH)_xO_2$ solid solutions. Consequently, the water solubility in Al-bearing α-PbO_2-TiO_2 is at least one order of magnitude greater than those in rutile- and $CaCl_2$-phases, making TiO_2 a significant water carrier at the pressure-temperature (*P–T*) conditions in the mantle transition zone (410 to 660 km depth in deep Earth's interior), when coexisting with Al^{3+} and Fe^{3+}. High-*P* and high-*T* Raman spectra were collected for these synthetic samples. The $CaCl_2$- and α-PbO_2-type phases irreversibly transform to a rutile-type structure at 950 K and ambient pressure. A reversible α-PbO_2 → baddeleyite phase transition in TiO_2 is detected at approximately P = 10 GPa and T = 300 K, and the incorporation of smaller amounts of Al^{3+} cations postpones the phase transition pressure. The lattice vibrational modes typically shift to lower frequencies at elevated temperature and to higher frequencies with increasing pressure due to variations in Ti(Al)-O bond length with temperature or pressure. Fourier transform infrared (FTIR) spectroscopic measurements were conducted on the samples under high-*T* or high-*P* conditions. Both *T*- and *P*-dependences are negative for the OH stretching vibrations in these TiO_2 polymorphs, except that the OH bands in the α-PbO_2-type samples exhibit a blueshift at elevated temperature. A negative linear correlation can be drawn between the measured OH stretching frequencies and the incorporated $M^{3+}O_6$ quadratic elongation, which were

computed based on first-principles calculations. The local octahedral distortion can provide useful insights for understanding the M^{3+} and H^{+} incorporation mechanism in TiO_2 and SiO_2 structures.

Keywords: TiO_2 polymorphs, Al-H coupled substitution, structure refinement, OH stretching vibration, octahedral distortion

1. Introduction

Rutile is the most common and stable TiO_2 mineral found in igneous and metamorphic rocks, like eclogite (McQueen et al. 1967; Dachille et al. 1968; Linde and DeCarli et al. 1969; Fahmi et al. 1993; Sobolev and Yefimova 2000; Zack et al. 2002). As an important nominally anhydrous minerals (NAMs), rutile can contain significant amounts of water, as high as a few thousand parts per million by weight (ppmw), when coupled with Nb^{5+} and Ta^{5+} incorporations (Vlassopoulos et al. 1993; Johnson 2006). On the other hand, pressure-induced phase transitions in TiO_2 systems have also been extensively studied (Sato et al. 1991; Gerward and Olsen 1997; Arlt et al. 2000; Swamy et al. 2002; Al-Khatatbeh et al. 2009), and the general phase sequence observed by experiments is summarized as follows: rutile (tetragonal in the symmetry of $P4_2/mnm$) → α-PbO_2 (orthorhombic, *Pbcn*) → baddeleyite (monoclinic, $P2_1/c$) → orthorhombic I (orthorhombic, *Pbca*) → orthorhombic II (cotunnite-type, orthorhombic, *Pnma*).

This is the peer-reviewed, final accepted version for American Mineralogist, published by the Mineralogical Society of America.
The published version is subject to change. Cite as Authors (Year) Title. American Mineralogist, in press.
DOI: https://doi.org/10.2138/am-2024-9316. http://www.minsocam.org/

58 TiO_2 polymorphs provide particular analogues for studying the SiO_2 system (e.g.,
59 Olsen et al. 1999; Meinhold 2010), among which the rutile, $CaCl_2$- and α-PbO_2-type SiO_2
60 polymorphs are relevant to the P–T conditions of the mantle. In the rutile structure (**Fig.**
61 **1a**), the TiO_6 octahedra stack parallel to the c axis by sharing the O-O edge along the
62 [110] direction (Rossman and Smyth 1990; Howard et al. 1991; Sugiyama and Takeuchi
63 1991; Swope et al. 1995). The Ti-O bonds can be categorized into two groups: four short
64 bonds inside the (110) plane and two long bonds perpendicular to the (110) plane. The
65 rutile → $CaCl_2$ ($P2_1nm$, **Fig. 1b**) phase transition is displacive and reversible at high
66 pressures (Oganov et al. 2005; Buchen et al. 2018; Fischer et al. 2018) by slightly tilting
67 the TiO_6 octahedra and splitting the a and b axes. The incorporation of Al^{3+} can stabilize
68 $CaCl_2$-type TiO_2 (Escudero et al. 2012) and SiO_2 (Ishii et al. 2022) when quenched to
69 ambient conditions. The $CaCl_2$-type structure is also widely found in many other oxides,
70 including SnO_2 (Suito et al. 1975), SiO_2 (Tsuchida and Yagi 1989; Murakami et al. 2003),
71 GeO_2 (Haines et al. 2000) and RuO_2 (Ono and Mibe 2011). The rutile → α-PbO_2 (**Fig. 1c**)
72 phase transition is reconstructive and typically occurs above 8 GPa and $T > 873$ K in TiO_2
73 (Olsen et al. 1999) but above 110 GPa in SiO_2 (e.g., Hirose et al. 2005). Additionally,
74 α-PbO_2-TiO_2 samples discovered in garnets have been used as pressure indicators in
75 ultrahigh-pressure metamorphism (Hwang et al. 2000; Goresy et al. 2001).

76 Hydration in stishovite (rutile-type SiO_2) and post-stishovite ($CaCl_2$-type SiO_2) has

also been widely studied for mineralogical and geophysical interests (Pawley et al. 1993; Litasov et al. 2007; Nisr et al. 2020; Lin et al. 2020, 2022; Ishii et al. 2022; Li et al. 2023); however, the hydration mechanisms inside the crystal structures still deserve further exploration. Taking advantage of multi-anvil press, we synthesized hydrous $CaCl_2$- and α-PbO_2-TiO_2 phases with various Al^{3+} concentrations. Using single-crystal X-ray diffraction (XRD) and Raman and FTIR vibrational spectroscopy techniques, the hydrogen behavior in TiO_2 polymorphs was systematically investigated, providing new insight into hydrous SiO_2 polymorphs as isostructural analogues.

2. Experimental methods and results

2.1 Sample Synthesis

To synthesize high-pressure TiO_2 polymorphs with various aluminum and water concentrations, two mixtures were prepared as the starting materials, namely, 95 wt.% TiO_2 + 5 wt.% Al_2O_3 and 93 wt.% TiO_2 + 7 wt.% $Al(OH)_3$, and the Al/(Al+Ti) molar percentages were approximately 7.5 mol.%. The chemical reagents TiO_2 (purity > 99.99 %, grain sizes < 0.5 μm), Al_2O_3 (purity > 99.7 %, grain sizes < 0.5 μm) and $Al(OH)_3$ (purity > 99.7 %, grain sizes < 0.6 μm) were purchased from Sinopharm Chemical Reagent Limited Corporation, Shanghai, China. The mixture was ground with ethanol for at least 3 h in a mortar and then dried in a glove box at 150 °C for at least 12

h.

The samples were synthesized utilizing a 1000-ton Walker-type multi-anvil press, and the synthetic pressure–temperature–duration (t) conditions are listed in **Table 1**. In each experimental run, the mixture was loaded in a platinum capsule (length = 2 mm, outer diameter = 2 mm and thickness = 0.2 mm) with both ends sealed by an electric spot welder, and 1 μL of distilled H_2O was added to the starting material to guarantee saturated water fugacity. The 14/8 assemblages (i.e., 14-mm periclase octahedra and 25.4-mm tungsten carbide anvils with 8-mm corner truncations) were adopted to synthesize the $CaCl_2$-type samples at P = 7 GPa and T = 1373 K, and three α-PbO_2-type phases were synthesized inside the 10/5 assemblages at P = 14 GPa and T = 1673 K. After each run, the Pt capsule was checked to ensure that there was no leakage under microscope, and the synthetic crystals were colorless with diameters typically in the range of 30~100 μm. For comparison, we also synthesized a rutile sample in a muffle furnace at T = 1873 K and ambient pressure from a mixture of TiO_2 + Al_2O_3, which was also loaded inside a two-way welded Pt capsule. The sizes of the grown crystals were typically 40~60 μm after the high-T treatment. In addition, Raman scans have also been performed throughout all the Pt capsule chambers with a spatial resolution of 2 μm, while only one TiO_2 phase is identified in each of the product.

This is the peer-reviewed, final accepted version for American Mineralogist, published by the Mineralogical Society of America.
The published version is subject to change. Cite as Authors (Year) Title. American Mineralogist, in press.
DOI: https://doi.org/10.2138/am-2024-9316. http://www.minsocam.org/

2.2 Composition analysis and structure refinement

Three to five selected chips from each product source were mounted in epoxy and polished on the surfaces. The chemical compositions were characterized by using electron probe microanalysis (EPMA) on a JEOL JXA 8100 with an accelerating voltage of 15 *kV*, a beam current of 20 *nA*, and a spot size of 5 μm to minimize fluctuations in the X-ray intensity and damage to the sample surface. The ZAF scheme, where Z represents the atomic number effect, A is the absorption, and F is the fluorescence, was used for correction, and pyrophanite and spinel standards were adopted to calibrate the Ti and Al concentrations, respectively. Three to five spots at different locations were measured on each crystal, with a total of 12~18 points for each sample. The average weight percentages for TiO_2 and Al_2O_3 with standard deviations are listed in **Supplemental Table S1**.

Clean crystals in diameters of 30~50 μm, without any inclusions under microscope, were chosen for single-crystal XRD measurements on a Bruker D8 QUEST 4-axis motor-driven diffractometer. The diffractometer was equipped with a PHOTON III C14 detector and a rotating silver-anode X-ray generator ($K_{\alpha\_average}$ = 0.56086 Å) operating at 50 kV and 0.9 mA. The intensity data were collected in a 2θ range up to 80°. The crystal structures were refined using the program SHELXL refinement package (Sheldrick 2015) inside the software package CrysAlisPro/Olex2 (Dolomanov et al. 2009). The intensity

data collection and unit-cell parameters are listed in **Table 2**. For each crystal in the $CaCl_2$- or α-PbO_2-type structure, more than 2000 reflections were collected for structure refinement. Their R_1 factors are smaller than 3.7 % for $I > 2\sigma$, and the R_{int} and goodness-of-fit (GooF) values are distributed in the ranges of 3.7~6.2 % and 1.06~1.19, respectively.

2.3 High-temperature Raman and FTIR spectra

Raman measurements of the samples were carried out using a Horiba LabRAM Evolution instrument with a microconfocal spectrometer, and a Nd:YAG laser source was excited at P = 20 mW with a wavelength of 532 nm and a spot size of approximately 1.5 μm. Spectra were collected in the range of 50~1000 cm^{-1} for the lattice vibrations, which were initially calibrated by a silicon crystal. For high-T and low-T measurements, the sample chips were loaded on sapphire windows in the Linkam TS 1500 heating stage and Linkam THMS 600 heating/cooling stage (Linkam Scientific Instruments Ltd., Tadworth, Surrey, UK), respectively. The highest temperature of 1473 K was achieved by resistance heating for rutile-type TiO_2 without any phase transition, and the lowest temperature of 100 K was reached by cooling with liquid nitrogen. The temperature was controlled by a commercial auto-controlling unit with an uncertainty within ±3 K, and the heating rate was set to 10 K/min with an interval of 50 K. The target temperature was first maintained

for 5 min for thermal equilibrium at each step. This heating strategy was also adopted in the following high-temperature FTIR measurements, and nitrogen was utilized as the protective gas in the sample chamber during the heating procedures. Each Raman spectrum was obtained in the backscattering direction through a VIS LWD 50× objective with an accumulation of 3 times and a total duration of 10 min.

To analyze the water contents in the products, 5~7 crystals (with diameters greater than 50 μm) from each source were selected for mid-FTIR measurements at ambient temperature. First, the chips were double-sided polished to a thickness of 30~50 μm, and then, unpolarized FTIR spectra were measured in transmission mode on a Nicolet iS50 FTIR instrument (Thermo Fisher, Madison, WI, USA), which was coupled with a continuum microscope, a KBr beam splitter, and an MCT-A detector cooled by liquid N_2. The spectra were collected in the wavenumber range of 2000~4000 cm^{-1} for the OH stretching vibration, with an accumulation of 128 scans and a resolution of 4 cm^{-1}, and the background was also measured after each measurement. For *in situ* high-*T* FTIR measurements, clean crystals were loaded on the sapphire window of a customized HS1300G-MK2000 external heating stage (INSTC, Boulder, CO, USA). The temperatures were also controlled by an auto-controlling unit, and dehydration was observed at approximately 1300 K for the rutile sample at ambient pressure.

This is the peer-reviewed, final accepted version for American Mineralogist, published by the Mineralogical Society of America.
The published version is subject to change. Cite as Authors (Year) Title. American Mineralogist, in press.
DOI: https://doi.org/10.2138/am-2024-9316. http://www.minsocam.org/

2.4 Vibrational spectra at high pressures

High-pressure Raman and FTIR measurements were conducted inside shortened symmetric diamond-anvil cells (DACs) (Zhu et al. 2023). Two IIa-type diamonds with 400 μm culets were loaded on hexagonal tungsten carbide seats and aligned at the centers of the piston and cylinder sides of a DAC, and the intensity ratios are greater than 2.0 between the 2nd-order C-C stretching band and background.

Rhenium gaskets were preindented to a thickness of 35~45 μm, and 280 μm-diameter holes were drilled at the centers of the indentations. A sample crystal (with a diameter in the range of 30~50 μm) was loaded inside the chamber hole, together with 1 or 2 annealed ruby chips (with a diameter within 5 μm) as the pressure gauge (Mao et al. 1986; Ye et al. 2018). Argon was cryogenically loaded inside the DAC chamber by cooling from liquid N_2, serving as the pressure transmitting medium. The sealing pressures were typically 1~2 GPa at room temperature, and the holes typically shrunk by 20~30 % in diameter after gas loading.

Vibrational spectra were collected up to ~20 GPa, with an interval of 1~2 GPa, and the pressure gradients in the Ar medium should be within 0.2 GPa throughout the experimental *P*-range at room temperature (Klotz et al. 2009). Each Raman spectrum was collected for a total duration of 20 min and an accumulation of 3 times, and FTIR spectra were obtained with an accumulation of 256 scans through the diamond windows. For

both the Raman and FTIR spectra, the peaks were fitted by the software package Peakfit v4.12 (Sea Solve Software, Inc., Massachusetts, USA). The backgrounds were treated as straight line segments in the Raman spectra from 50 to 1000 cm^{-1}.

3. Results and Discussion

3.1. Lattice and OH stretching vibrations in TiO_2 polymorphs

Representative Raman and FTIR spectra of the synthetic samples obtained under ambient conditions are shown in **Fig. 2(a,b)**, respectively. There are 15 irreducible optical modes in rutile with 6 atoms (2 TiO_2 formulae) per unit cell (Balachandran and Eror 1982): $\Gamma = A_{1g}(R) + A_{2g}(ia) + B_{1g}(R) + B_{2g}(R) + E_g(R) + A_{2u}(IR) + 2B_{1u}(ia) + 3E_u(IR)$, where the items '*R*', '*IR*' and '*ia*' denote the Raman-active, IR-active and inactive modes, respectively. The vibrational modes at 142 (B_{1g} for TiO_6 rotation around the *c* axis), 439 (E_g, O-Ti-O bending) and 607 cm^{-1} (A_{1g}, asymmetric Ti-O stretching) are observed for this rutile sample, together with the multiphonon process at 240 cm^{-1}, which is consistent with previous studies (Frank et al. 2012; Lan et al. 2012). In the $CaCl_2$-type structure, the weak B_{1g} peak appears as a broader peak at a lower frequency of approximately 110 cm^{-1}, which makes the distinction between the rutile and $CaCl_2$-TiO_2 phases from the Raman spectra (Zhou et al. 2009; Zhang et al. 2019). However, the frequential differences for other bands are typically within 5 cm^{-1} between the samples in the rutile and $CaCl_2$

structures.

Besides, there are 12 atoms (4 formulae) in a α-PbO_2-type primitive cell, and the factor group analysis gives attributions of the 33 irreducible optical modes (Cai et al. 2011): $\Gamma = 4B_{1u}(IR) + 3B_{2u}(IR) + 4B_{3u}(IR) + 4A_g(R) + 5B_{1g}(R) + 4B_{2g}(R) + 5B_{3g}(R) + 4A_u(ia)$. The following bands are indexed in the Raman spectrum for the α-PbO_2-TiO_2 sample: A_g (at 170, 425 and 530 cm^{-1}), B_{1g} (at 282, 315, 354 and 569 cm^{-1}), B_{2g} (at 340 and 816 cm^{-1}) and B_{3g} (at 148 and 607 cm^{-1}). These bands are generally consistent with the theoretical calculations (Cai et al. 2011) and spectroscopic measurements (Mammone et al. 1981; Goresy et al. 2001; Tan et al. 2018), except that a few weak bands cannot be detected in this study. When smaller Al^{3+} cations substitute into the lattice structure, the Raman peaks shift to higher frequencies, with increments typically within 10 cm^{-1} for these samples.

The OH stretching bands for the rutile sample are observed at 3277 and 3323 cm^{-1} (**Fig. 2b**) and are attributed to the reduction of Ti^{4+} ($Ti^{4+} \rightarrow Ti^{3+} + H^+$) and Al^{3+}-H^+ coupled substitution ($Ti^{4+} \rightarrow Al^{3+} + H^+$), respectively (Bromiley and Hilairet 2005; Wang et al. 2023). OH stretching absorbances are observed at approximately 3317 and 2925 cm^{-1} for the $CaCl_2$-type and α-PbO_2-type phases, respectively. Similarly, the main OH bands for α-PbO_2-$Ti_{1-x}(FeH)_xO_2$ ($0.38 < x < 0.76$) were also measured around 2860~2870 cm^{-1} (Nishihara and Matsukage 2016), and the correlation between OH stretching

This is the peer-reviewed, final accepted version for American Mineralogist, published by the Mineralogical Society of America.
The published version is subject to change. Cite as Authors (Year) Title. American Mineralogist, in press.
DOI: https://doi.org/10.2138/am-2024-9316. http://www.minsocam.org/

frequencies and local structures associated with Al^{3+} substitution is discussed in the following sections.

3.2. Aluminum and hydrogen incorporations

The water concentrations (in the unit of mol·L^{-1} for C_{H2O}) in these synthetic samples can be derived based on the Lambert–Beer Law as follows:

$$C_{H_2O} = \frac{1}{\varepsilon \times \gamma \times d} \int \left(\frac{I_0(v)}{I(v)} \right) dv \quad (1)$$

where ε is the absorption coefficient, d (in cm) is the thickness of the double-sided polished sample, and the orientation factor γ is assumed to be 1/3. $I_0(v)$ and $I(v)$ are the intensities of the transmitted and incident light, respectively. We adopted both the absorption coefficients for rutile-TiO_2 from Maldener et al. (2001) (3.8×10^4 L·mol^{-1}·cm^{-2}) and Johnson et al. (1973) (3.02×10^4 L·mol^{-1}·cm^{-2}) for calculating C_{H2O} among the TiO_2 polymorphs since variations in their densities are generally within 2 % (**Table 2**). Besides, the water content C (H/10^6 Si) can be also calculated based on the calibration by Paterson (1982):

$$C = \frac{X_i}{150 \cdot \xi} \cdot \int \frac{K(\bar{v}) \cdot d\bar{v}}{3780 - \bar{v}} \quad (2)$$

where ξ is an orientation factor for unpolarized spectra. The density factor X_i is equal to $10^6 \cdot (M/d)$, where M (g/mol) and d (g/L) are the molar mass and density of the mineral, respectively (Bolfan-Casanova et al. 2000). The estimated water concentrations are listed

This is the peer-reviewed, final accepted version for American Mineralogist, published by the Mineralogical Society of America.
The published version is subject to change. Cite as Authors (Year) Title. American Mineralogist, in press.
DOI: https://doi.org/10.2138/am-2024-9316. http://www.minsocam.org/

in **Table 2** and are based on both the Lambert–Beer Law and Paterson's calibration.

The water content in the rutile-type sample, synthesized at ambient pressure, is 330~420 H/10^6 Si according to the Lambert–Beer calibration, which might come from absorbed H_2O molecules in the atmosphere during sample loading in the Pt capsule. Its Al^{3+} concentration is also very low (Al/(Al+Ti) = 0.2 mol.%), and increasing pressure has a positive contribution to the incorporations of both Al^{3+} (Slepetys and Vaughan 1969; Escudero et al. 2012; Hoff and Watson 2021) and H^+ (Johnson 2006) in rutile. The H^+ population in the $CaCl_2$-type sample synthesized from $Al(OH)_3$ was approximately 5 times greater than that in the sample synthesized from Al_2O_3, although both samples were synthesized under the same *P–T* conditions. Hence, the OH^- groups in $Al(OH)_3$ hydroxide may play an important role in H^+ substitution.

Moreover, the H^+ molar concentrations (molar percentages) in the rutile- and $CaCl_2$-type samples are typically one or two orders lower in magnitude than those for Al^{3+}; hence, the dominant Al^{3+} substitution form in both the phases should be $3Ti^{4+} = 4Al^{3+}$ (Gesenhues and Rentschler 1999; Stebbins 2007; Escudero et al. 2011, 2012; Wang et al. 2023) instead of $Ti^{4+} = Al^{3+} + H^+$. Thus, the formula can be simplified as rutile-$Ti_{0.998}Al_{0.002}O_2$, $CaCl_2$-$Ti_{0.961}Al_{0.053}O_2$ and $CaCl_2$-$Ti_{0.972}Al_{0.037}O_2$, assuming that the oxygen sites have fully occupied the $CaCl_2$-type structures synthesized at a pressure of 7 GPa (Bak et al. 2006; Erdal et al. 2010). Notably, the Al^{3+} molar percentages are also

267 significantly greater than those of H^+ in the rutile-SiO_2 (Pawley et al. 1993; Chung and
268 Kagi 2002; Litasov et al. 2007) and $CaCl_2$-SiO_2 (Ishii et al. 2022) samples.

269 In contrast, the water concentrations in the Al-bearing α-PbO_2-type samples are
270 0.4~0.5 and 0.7~0.8 wt.%, which are 1 order of magnitude greater than those in
271 $CaCl_2$-$Ti_{0.972}Al_{0.037}O_2$. The H:Al molar ratios are 1.07~1.12:1, 0.85~0.89:1 and
272 0.96~1.20:1 according to the calibrations from Maldener et al. (2001), Johnson et al.
273 (1973) and Paterson (1982), respectively, suggesting that the H^+ population is almost
274 equal to that of Al^{3+}. No OH stretching vibrational signal was detected in the infrared
275 spectrum for the Ti-pure α-PbO_2 phase (**Fig. 2b**), even though additional H_2O was added
276 to the starting mixture. Therefore, the dominant Al^{3+} substitution in the α-PbO_2-TiO_2
277 phases is coupled with H^+ ($Ti^{4+} = Al^{3+} + H^+$), forming solid solutions between TiO_2 and
278 AlOOH, and their formulae can be expressed as α-PbO_2-$Ti_{0.957}(AlH)_{0.043}O_2$ and
279 α-PbO_2-$Ti_{0.930}(AlH)_{0.070}O_2$, respectively. Nishihara and Matsukage (2016) also
280 synthesized $Ti_x(FeH)_{1-x}O_2$ solid solutions at P = 16 GPa and 1273 < T < 1873 K and
281 reported that the phases with x > 0.35 and x < 0.23 crystallized as α-PbO_2-type (*Pbcn*)
282 and ε-FeOOH ($P2_1nm$) structures, respectively. The TiO_2 and Fe_2O_3 compositions were
283 determined via scanning electron microscopy–energy dispersive X-ray spectrometry
284 (SEM–EDS) measurements, and the H_2O content was estimated from the total mass loss.
285

This is the peer-reviewed, final accepted version for American Mineralogist, published by the Mineralogical Society of America.
The published version is subject to change. Cite as Authors (Year) Title. American Mineralogist, in press.
DOI: https://doi.org/10.2138/am-2024-9316. http://www.minsocam.org/

3.3. Crystal structures

The incorporation of Al^{3+} in rutile may distort the tetragonal symmetry, yielding the orthorhombic $CaCl_2$ structure (**Fig. 1b**) (Escudero et al. 2012), which is isostructural with δ-AlOOH (Kuribayashi et al. 2014) and ε-FeOOH (Gleason et al. 2008; Thompson et al. 2020). The *b* axis was slightly shorter than the *a* axis, with differences within 0.2 % (**Table 2**). Wang et al. (2023) also synthesized rutile titanium dioxide with up to 4.7 mol.% Al, but at a relatively low pressure of 3 GPa (T = 1273 K); hence, synthetic pressure can also play an important role in forming a distorted $CaCl_2$ structure.

For Al^{3+} substitution ($3Ti^{4+} = 4Al^{3+}$) in the $CaCl_2$-type phases, three quarters of the Al^{3+} cations take the place of Ti^{4+} in the octahedral centers (Al^{oct}), and the remaining cations are located in the interstitial sites (Al^{int}) (Escudero et al. 2011, 2012; Hoff and Watson 2021). During the refinements of the $CaCl_2$-type structures, a strong Q peak was found for some unrecognized atoms approximately at (0.2, 0.5, 0), which was attributed to an interstitial Al site. In dry rutile-TiO_2 samples, two interstitial Al sites have been proposed at (0, 0.5, 0.25) and (0, 0.5, 0), the latter of which can be responsible for the rutile → $CaCl_2$ phase transition (Escudero et al. 2011). It is possible that incorporation of even a small number of protons can shift the interstitial Al^{3+} position in the lattice. Since the Al^{int} occupancies are rather small (< 0.7 %), the coordinates are fixed during structural refinements. The refined atomic positions for O^{2-} and Ti(Al) at the octahedral

This is the peer-reviewed, final accepted version for American Mineralogist, published by the Mineralogical Society of America.
The published version is subject to change. Cite as Authors (Year) Title. American Mineralogist, in press.
DOI: https://doi.org/10.2138/am-2024-9316. http://www.minsocam.org/

site are listed in **Table 3**, and the Ti and Al occupancies are calculated based on the EPMA measurements with a ratio of (Ti + Al^{oct}) : O equal to 1 : 2. In addition, the refined anisotropic displacement parameters (U_{ij}, in units of $Å^2$) are listed in **Supplemental Table S2**. Considering the Al^{3+}-H^+ coupled substitution, the Al^{3+} cations in the α-PbO_2-type phases essentially concentrate at the octahedral sites. However, the proton positions cannot be precisely refined based on the single-crystal XRD measurements.

The average Ti(Al)-O bond and O-O edge lengths in the $Ti(Al)O_6$ octahedra (**Table 4**) were calculated utilizing the software package Xtaldraw (Downs et al. 1993). The unit-cell and octahedral volumes decrease at elevated Al^{3+} concentrations among rutile-$Ti_{0.998}Al_{0.002}O_2$, $CaCl_2$-$Ti_{0.972}Al_{0.037}O_2$ and $CaCl_2$-$Ti_{0.961}Al_{0.053}O_2$ since the radius of Al^{3+} (0.535 Å) is smaller than that of Ti^{4+} (0.605 Å) (Shannon 1976). A similar effect of Al on the unit-cell volume was also observed for dry rutile-type samples (Gesenhues and Rentschler 1999; Escudero et al. 2012). In addition, the unite-cell and octahedral volumes for the α-PbO_2 phases increase in the order of $Ti_{0.957}(AlH)_{0.043}O_2$ < TiO_2 < $Ti_{0.930}(AlH)_{0.070}O_2$, and the incorporation of H^+ should have a positive contribution to the volume of rutile instead (Hoff and Watson 2021; Wang et al. 2023).

3.4. OH stretching frequency *versus* octahedral distortion

Wang et al. (2023) synthesized several M^{3+}-doped rutile samples (M = Al, Ga, Fe, Cr,

This is the peer-reviewed, final accepted version for American Mineralogist, published by the Mineralogical Society of America.
The published version is subject to change. Cite as Authors (Year) Title. American Mineralogist, in press.
DOI: https://doi.org/10.2138/am-2024-9316. http://www.minsocam.org/

and Ti^{3+} for Ti^{4+} = Ti^{3+} + H^{+} substitution in hydrous rutile). The OH stretching frequencies measured by FTIR spectroscopy (cm^{-1}) are negatively linearly correlated with the theoretically calculated $M^{3+}O_6$ distortion, which is defined as (M-O_2 – M-O_1)/M-O_1 (where M-O_1 and M-O_2 are the short and long M^{3+}-O^{2-} bond lengths, respectively, in a local $M^{3+}O_6$ octahedron). Single-crystal XRD experiments can only reveal the average Ti(Al)-O bond lengths in a bulk lattice structure. In this discussion, we adopt the first-principles calculation method (**Supplemental Section S1**) to compute the Al-O bond lengths for the local $Al^{3+}O_6$ octahedra in the hosts of $CaCl_2$-TiO_2, α-PbO_2-TiO_2, rutile-SiO_2 and $CaCl_2$-SiO_2 (**Supplemental Table S3**).

The correlation between the OH stretching frequency (v_i) and the local octahedral distortion inside various TiO_2 and SiO_2 hosts was further investigated, and a more general octahedral distortion expression, quadratic elongation $<\lambda>$ (Robinson et al. 1971; Hazen et al. 2000), was adopted to evaluate local $Al^{3+}O_6$ distortions in various hosts:

$$< \boldsymbol{\lambda} >= \sum_{\boldsymbol{i=1}}^{\boldsymbol{6}}[(\boldsymbol{l_i}/\boldsymbol{l_0})^{\boldsymbol{2}}/\boldsymbol{n}] \quad \textbf{(3)}$$

where l_0 is the distance from the center to the vertex in a regular octahedron of the same volume and l_i is the distance from the central Al^{3+} to the i-th O^{2-}. The quadratic elongations are 1.00061~1.00069 for the $M^{3+}O_6$-octahedra in the rutile and $CaCl_2$-TiO_2 hosts; 1.00108~1.00119 for AlO_6 in the rutile and $CaCl_2$-SiO_2 hosts; and 1.00154 and 1.00185 for the AlO_6 and $Fe^{3+}O_6$ in the α-PbO_2-TiO_2, respectively. A larger $<\lambda>$ value

This is the peer-reviewed, final accepted version for American Mineralogist, published by the Mineralogical Society of America.
The published version is subject to change. Cite as Authors (Year) Title. American Mineralogist, in press.
DOI: https://doi.org/10.2138/am-2024-9316. http://www.minsocam.org/

corresponds to an octahedron with more significant distortion.

The OH stretching vibrational frequencies are measured for the Al-bearing $CaCl_2$-TiO_2 (~ 3318 cm^{-1}) and α-PbO_2-TiO_2 (~ 2925 cm^{-1}) samples in this study, and those for M^{3+}-doped rutile-TiO_2 samples (M = Al, Ga, Fe, Cr, and Ti^{3+}) are reported in Wang et al. (2023). The strongest OH bands in the rutile-SiO_2, $CaCl_2$-SiO_2 and α-PbO_2-$Ti_x(FeH)_{1-x}O_2$ phases are detected at approximately 3111 cm^{-1} (Pawley et al. 1993; Litasov et al. 2007), 3100 cm^{-1} (Ishii et al. 2022 for the sample with 0.86 wt.% H_2O), and 2862~2869 cm^{-1} (Nishihara and Matsukage 2016), respectively, which should be associated with the coupled substitution of $Si^{4+} = Al^{3+} + H^+$ or $Ti^{4+} = Fe^{3+} + H^+$.

A negative linear regression can be fitted between the measured OH stretching vibrational frequency and the calculated $M^{3+}O_6$ quadratic elongation among these phases (**Fig. 3**), with R^2 = 0.99. Many studies have attributed the OH stretching vibration associated with the substitution of $Ti^{4+} = M^{3+} + H^+$ to protonation around the (1/2, 1/2, 0) site along the shared O-O edge ($d_{O..O}$ = 2.53 Å) in the (110) plane, forming a non-colinear O-H…O configuration (Vlassopoulos et al. 1993; Swope et al. 1995; Bromiley and Hilairet 2005; Yang et al. 2011). This attribution is consistent with earlier polarized infrared spectroscopic measurements (Soffer 1961). If the local AlO_6 octahedron becomes more distorted in other hosts, then the O…O edge for protonation can be even shortened, and H^+ can be further pushed away from the edge. Subsequently, the covalent O-H bond

This is the peer-reviewed, final accepted version for American Mineralogist, published by the Mineralogical Society of America.
The published version is subject to change. Cite as Authors (Year) Title. American Mineralogist, in press.
DOI: https://doi.org/10.2138/am-2024-9316. http://www.minsocam.org/

becomes weakened, causing a redshift in the O-H stretching vibrational frequency. However, further investigations are still needed to determine the H positions in α-PbO_2- and $CaCl_2$-type hosts for both SiO_2 and TiO_2 systems.

3.5. Temperature effect on the lattice and OH stretching vibrations

The frequencies (v_i's) of the lattice (Raman-active) and OH stretching (IR-active) vibrations are fitted at various temperatures for these TiO_2 polymorphs. The representative high-T Raman and FTIR spectra with linear regressions between v_i's and T are exhibited in **Fig. 4(a-f)** and **Fig. 5(a-f)**, respectively, for rutile-$Ti_{0.998}Al_{0.002}O_2$, $CaCl_2$-$Ti_{0.972}Al_{0.037}O_2$ and α-PbO_2-$Ti_{0.930}(AlH)_{0.070}O_2$ as representatives, while in **Supplemental Fig. S1(a-f)** and **Fig. S2(a-f)**, individually, for the other samples. After each heating run, another quenched Raman or FTIR spectrum was also measured for comparison, as exhibited as gray curves in the figures. The fitted $\partial v_i/\partial T$ values (in $cm^{-1}\cdot K^{-1}$) are listed in **Supplemental Table S4**.

The $CaCl_2$- and α-PbO_2-type samples systematically transform to the rutile structure at approximately 950 K, as supported by both the high-T Raman and FTIR spectra. The weak B_{1g} mode shifts from ~ 140 cm^{-1} to ~ 160 cm^{-1} at 950 K for the $CaCl_2$-type samples (**Fig. 4(b,e)**), and their OH stretching bands also show an abrupt redshift of approximately 20 cm^{-1} (**Fig. 5(c,f)** and **Fig. S2(a,d)**). Upon the α-PbO_2 → rutile phase

This is the peer-reviewed, final accepted version for American Mineralogist, published by the Mineralogical Society of America.
The published version is subject to change. Cite as Authors (Year) Title. American Mineralogist, in press.
DOI: https://doi.org/10.2138/am-2024-9316. http://www.minsocam.org/

transition, the Raman patterns change completely and match well with those for the rutile structure (**Fig. 4(c,f)**), and the corresponding OH bands exhibit a blueshift of approximately 50 cm^{-1} (**Fig. 5(c,f)** and **Fig. S2(b,e)**). In addition, the quenched Raman and FTIR spectra for these $CaCl_2$- and α-PbO_2-type samples are also consistent with those for the rutile structure, suggesting that these temperature-induced phase transitions are irreversible.

The O-Ti-O bending (at 440 cm^{-1}) and asymmetric Ti-O stretching (at 610 cm^{-1}) modes in the rutile sample shift to lower frequencies at elevated temperature due to thermal expansion of the lattice structure, and the multiphonon process shifts to higher frequency since the anharmonic and disorder features have become more significant (Samara and Peercy 1973; Lan et al. 2012). A similar T effect on the vibrational behaviors is also observed for the $CaCl_2$-type samples before the phase transition (**Fig. 6a**), considering their structural similarity. The lattice modes in the α-PbO_2-type samples systematically shift to lower frequencies with increasing temperature below T = 950 K, and the decreasing rates are typically in the range of 0 ~ -0.05 $cm^{-1}\cdot K^{-1}$ among these polymorphs.

The OH stretching band at 3324 cm^{-1} in the spectrum of rutile-$Ti_{0.998}Al_{0.002}O_2$ shifts to a lower frequency with increasing temperature at a much quicker rate (-0.17 $cm^{-1}\cdot K^{-1}$) than that at 3278 cm^{-1} (-0.06 $cm^{-1}\cdot K^{-1}$) (**Fig. 5d**). Consequently, both peaks merge

together above 550 K. A negative *T*-dependence for the OH stretching modes is also observed for the $CaCl_2$-type samples before the phase transition, which is consistent with previous high-*T* vibrational measurements of rutile samples (Yang et al. 2011; Guo 2017; Wang et al. 2020). This phenomenon is attributed to thermal expansion of the covalent O-H bond (Yang et al. 2011), despite the expansion of the O…O edge for protonation at elevated temperature according to single-crystal XRD experiments (Meagher and Lager 1979; Sugiyama and Takéuchi 1991). As listed in **Table 4**, the O…O edge distances in the α-PbO_2-type phases are longer than that (2.53 Å) for protonation in the rutile- and $CaCl_2$-ype structures. It is possible that a normal O-H…O configuration could be formed in the α-PbO_2-type phases instead, which is almost linear, and the OH stretching frequency is positively correlated to the hydrogen bond length ($d_{O...H}$) (Libowitzky 1999). Consequently, the OH bands in the α-PbO_2-type samples shift to higher frequencies at elevated temperature, together with thermal expansion of the hydrogen bond.

3.6. Pressure dependence of vibrational modes

The high-pressure Raman spectra and variations in v_i's with pressure are illustrated in **Fig. 7(a-f)** for the representative samples of rutile-$Ti_{0.998}Al_{0.002}O_2$, $CaCl_2$-$Ti_{0.972}Al_{0.037}O_2$ and α-PbO_2-$Ti_{0.930}(AlH)_{0.070}O_2$, as well as in **Supplemental Fig. S3(a-d)** for α-PbO_2-TiO_2 and α-PbO_2-$Ti_{0.957}(AlH)_{0.043}O_2$. Considering the water

This is the peer-reviewed, final accepted version for American Mineralogist, published by the Mineralogical Society of America.
The published version is subject to change. Cite as Authors (Year) Title. American Mineralogist, in press.
DOI: https://doi.org/10.2138/am-2024-9316. http://www.minsocam.org/

solubility in the rutile phase and the sample thickness limitation inside the DAC chamber, we chose the natural rutile-$Ti_{0.988}Fe_{0.14}O_2$ sample with 510±120 ppmw. H_2O (Wang et al. 2020) for high-*P* FTIR measurements (**Fig. 8(a,d)**), and only one OH stretching band at 3280 cm^{-1} could be reasonably fitted only in the *P*-range up to 8 GPa. Moreover, FTIR spectra were also collected for $CaCl_2$-$Ti_{0.972}Al_{0.037}O_2$ (**Fig. 8(b,e)**) and α-PbO_2-$Ti_{0.930}(AlH)_{0.070}O_2$ (**Fig. 8(c,f)**) below P = 20 GPa.

The rutile → baddeleyite (ZrO_2) phase transition was detected in the rutile-$Ti_{0.998}Al_{0.002}O_2$ crystal when compressed to 10 GPa (**Fig. 7(a,d)**), as evidenced by the appearance of several sharp peaks, especially between 200 and 300 cm^{-1}. A similar phase transition was also detected at approximately 12~13 GPa for powder rutile-TiO_2 (Gerward and Olsen 1997) and polycrystalline anatase-TiO_2 (Arlt et al. 2000), as well as at 16 GPa for natural rutile-$Ti_{0.988}Fe_{0.011}O_2$ (Lu et al. 2023). In addition, in these studies, it was also reported that the baddeleyite-type structure further transforms to the α-PbO_2-type structure when decompressed to 7 GPa. In this study, the α-PbO_2 → baddeleyite phase transition is observed at P = 10 GPa for α-PbO_2-TiO_2 (**Fig. S3(a,d)**), while at P = 19 GPa, this transition occurs for α-PbO_2-$Ti_{0.957}(AlH)_{0.043}O_2$ (**Fig. S3(b,e)**) but not for $CaCl_2$-$Ti_{0.972}Al_{0.037}O_2$ (**Fig. 7(b,e)**) or α-PbO_2-$Ti_{0.930}(AlH)_{0.070}O_2$ (**Fig. 7(c,f)**) throughout the experimental *P*-range. Thus, this pressure-induced phase transition is reversible at ambient temperature, and doping Al^{3+} postpones it to higher pressures.

438 The lattice vibrational modes among these TiO_2 polymorphs shift to higher
439 frequencies at elevated pressure (**Supplemental Table S5**), except for a few weak bands
440 below 320 cm^{-1}, which are associated with rotations of the $Ti(Al)O_6$ units. The Ti(Al)-O
441 bonds strengthen during compression, as opposed to the thermal expansion procedure. A
442 positive correlation is generally observed between the magnitude of $\partial v_i/\partial P$ ($cm^{-1}\cdot GPa^{-1}$)
443 and the vibrational frequency v_i (**Fig. 9a**); hence, the Ti-O stretching modes are more
444 sensitive to pressure variation than are the O-Ti-O bending modes. The OH stretching
445 bands in the rutile, $CaCl_2$ and α-PbO_2 samples systematically redshift with increasing
446 pressure (**Fig. 9b**). High-pressure single-crystal XRD measurements of the rutile-TiO_2
447 samples indicated that the *a*-axis is more compressible than the *c*-axis (Hazen and Finger
448 1981; Kudoh and Takeda 1986) and that the shared O-O edge in the [110] direction is
449 significantly compressed, pushing protons further away from the edge. Then, the O-H
450 interaction also weakens during compression. Besides, the OH stretching frequency in the
451 α-PbO_2-type structure also exhibit red-shift at high pressure due to compression of O…H
452 bond, which is consistent with its behavior at high temperature as mentioned above.
453
454 **4. Implications**
455 According to the *P–T* phase diagram in TiO_2 (Olsen et al. 1999), the α-PbO_2-type
456 phase becomes stable above 4 GPa (below 120 km depth) along the normal mantle

This is the peer-reviewed, final accepted version for American Mineralogist, published by the Mineralogical Society of America.
The published version is subject to change. Cite as Authors (Year) Title. American Mineralogist, in press.
DOI: https://doi.org/10.2138/am-2024-9316. http://www.minsocam.org/

457 geotherm (Turcotte and Schubert 2002) and should constitute a stable TiO_2 structure in
458 the mantle transition zone (between the 410- and 660-km seismic discontinuities), as well
459 as part of the lower mantle before the α-PbO_2 → baddeleyite phase transition. The
460 Al^{3+}-H^+ coupled substitution in α-PbO_2-TiO_2 ($Ti^{4+} = Al^{3+} + H^+$, forming $Ti_x(AlH)_{1-x}O_2$
461 solid solutions) is quite different from that in the $CaCl_2$- and rutile-type structures ($3Ti^{4+}$
462 $= 4Al^{3+}$). Consequently, the water solubility in Al-bearing α-PbO_2-TiO_2 is much greater
463 than that in the $CaCl_2$ phase. Nishihara and Matsukage (2016) also synthesized
464 $Ti_x(FeH)_{1-x}O_2$ ($0.15 < x < 0.75$) solid solutions at $P = 16$ GPa and $1273 < T < 1873$ K.
465 Hence, α-PbO_2-type TiO_2 could retain significant amounts of water (at the wt.% level) in
466 the presence of trivalent cations such as Al^{3+} and Fe^{3+}, despite the limited TiO_2 contents
467 in mid-oceanic basalts (Gale et al. 2013; White and Klein 2014).

468 Moreover, isostructural TiO_2 polymorphs are important analogs of the SiO_2 system.
469 Previous experiments have indicated that the incorporation of Al^{3+} can significantly
470 enhance H_2O solubility in stishovite, up to approximately 3000 ppmw. (Pawley et al.
471 1993; Chung and Kagi 2002; Litasov et al. 2007). Hence, Al-bearing stishovite can be an
472 important water carrier in eclogite (a typical basaltic composition) above 10 GPa (Hirose
473 and Fei 2002; Litasov et al. 2004). Ishii et al. (2022) synthesized Al-bearing
474 post-stishovite phases at $24 < P < 28$ GPa and $1973 < T < 2273$ K, with water contents as
475 high as 1.1 wt.%. These Al-doped $CaCl_2$-SiO_2 samples can even be quenched to ambient

conditions, and the presence of Al^{3+} significantly reduces the rutile → $CaCl_2$ phase transition pressure in SiO_2 (e.g., Lakshtanov et al. 2007; Fischer et al. 2018; Criniti et al. 2023). As inferred from this study, seifertite (α-PbO_2-SiO_2), a major mineral in basalts at the bottom of the lower mantle (20~25 wt.% above 110 GPa; e.g., Irifune et al. 1986; Murakami et al. 2003; Hirose et al. 2005), may also contain even more water when coupled with Al^{3+} incorporation. In addition, the local $M^{3+}O_6$ distortion from theoretical calculations has been successfully utilized to explain the different OH stretching frequencies measured in various TiO_2 and SiO_2 hosts, as well as the incorporated M^{3+} concentrations in rutile-TiO_2 samples (Wang et al. 2023). Therefore, local octahedral distortion should be relevant and important for understanding both M^{3+} and H^+ substitutions in AO_2-type (A = Si, Ti) minerals, as well as hydrogen bonding behavior in lattices under high-T and high-P conditions.

Acknowledgment: This work was supported by the National Natural Science Foundation of China (42072050, 42302040) and the National Key Research and Development Program of China (Grant No. 2018YFA0702700).

References:

Goresy, A.E., Chen, M., Gillet, P., Dubrovinsky, L.S., Graup, G., and Ahuja, R. (2001) A

natural shock-induced dense polymorph of rutile with α-PbO_2 structure in the suevite from the Ries crater in Germany. Earth and Planetary Science Letters, 192(4), 485–495. https://doi.org/10.1016/s0012-821x(01)00480-0.

Al-Khatatbeh, Y., Lee, K.K.M., and Kiefer, B. (2009) High-pressure behavior of TiO_2 as determined by experiment and theory. Physical Review B, 79(13), 134114. https://doi.org/10.1103/PhysRevB.79.134114.

Arlt, T., Bermejo, M., Blanco, M.A., Gerward, L., Jiang, J.Z., Olsen, J.S., and Recio, J.M. (2000) High-pressure polymorphs of anatase TiO_2. Physical Review B, 61(21), 14414. https://doi.org/10.1103/PhysRevB.61.14414.

Bak, T., Nowotny, J., and Nowotny, M.K. (2006) Defect disorder of titanium dioxide. The Journal of Physical Chemistry B, 110(43), 21560–21567. https://doi.org/10.1021/jp063700k.

Balachandran, U. and Eror, N.G. (1982) Raman spectra of titanium dioxide. Journal of Solid State Chemistry, 42, 276–282. https://doi.org/10.1016/0022-4596(82)90006-8.

Bolfan-Casanova, N., Keppler, H., and Rubie, D.C. (2000) Water partitioning between nominally anhydrous minerals in the MgO-SiO_2-H_2O system up to 24 GPa: implications for the distribution of water in the Earth's mantle. Earth and Planetary Science Letters, 182, 209–221. https://doi.org/10.1016/S0012-821X(00)00244-2.

Bromiley, G.D. and Hilairet, N. (2005) Hydrogen and minor element incorporation in

synthetic rutile. Mineralogical Magazine, 69(3), 345–358. https://doi.org/10.1180/0026461056930256.

Buchen, J., Marquardt, H., Schulze, K., Speziale, S., Ballaran, T.B., Nishiyama, N., and Hanfland, M. (2018) Equation of state of polycrystalline stishovite across the tetragonal-orthorhombic phase transition. Journal of Geophysical Research, 123, 7347–7360. https://doi.org/10.1029/2018JB015835.

Cai, Y., Zhang, C., and Feng, Y.P. (2011) Dielectric properties and lattice dynamics of α-PbO_2-type TiO_2: The role of soft phonon modes in pressure-induced phase transition to baddeleyite-type TiO_2. Physical Review B, 84(9), 094107. https://doi.org/10.1103/PhysRevB.84.094107.

Chung, J.I. and Kagi, H. (2002) High concentration of water in stishovite in the MORB system. Geophysical Research Letters, 29, 2020. https://doi.org/10.1029/2002gl015579.

Dachille, F., Simons, P.Y., and Roy, R. (1968) Pressure-temperature studies of anatase, brookite, rutile and TiO_2-II. American Mineralogist, 53(11-12), 1929–1939.

Dolomanov, O.V., Bourhis, L.J., Gildea, R.J., Howard, J.A., and Puschmann, H. (2009) OLEX2: a complete structure solution, refinement and analysis program. Journal of Applied Crystallography, 42(2), 339–341. https://doi.org/10.1107/S0021889808042726.

533 Downs, R.T., Bartelmehs, K.L., Gibbs, G.V., and Boisen, M.B. (1993) Interactive
534 software for calculating and displaying X-ray or neutron powder diffractometer
535 patterns of crystalline materials. American Mineralogist, 78(10), 1104–1107.
536 Erdal, S., Kongshaug, C., Bjorheim, T.S., Jalarvo, N., Haugsrud, R., and Norby, T. (2010)
537 Hydration of rutile TiO_2: Thermodynamics and effects on n- and p-type electronic
538 conduction. The Journal of Physical Chemistry C, 114, 9139–9145.
539 https://doi.org/10.1021/jp101886a.
540 Escudero, A., Delevoye, L., and Langenhorst, F. (2011) Aluminum incorporation in TiO_2
541 rutile at high pressure: An XRD and high-resolution ^{27}Al NMR study. The Journal
542 of Physical Chemistry C, 115(24), 12196–12201. https://doi.org/10.1021/jp202930r.
543 Escudero, A., Langenhorst, F., and Müller, W.F. (2012) Aluminum solubility in TiO_2
544 rutile at high pressure and experimental evidence for a $CaCl_2$-structured polymorph.
545 American Mineralogist, 97(7), 1075–1082. https://doi.org/10.2138/am.2012.4049.
546 Fahmi, A., Minot, C., Silvi, B., and Causá, M. (1993) Theoretical analysis of the
547 structures of titanium dioxide crystals. Physical Review B, 47(18), 11717.
548 https://doi.org/10.1103/PhysRevB.47.11717.
549 Fischer, R.A., Campbell, A.J., Chidester, B.A., Reaman, D.M., Thompson, E.C., Pigott,
550 J.S., Prakapenka, V.B., and Smith, J.S. (2018) Equations of state and phase
551 boundary for stishovite and $CaCl_2$-type SiO_2. American Mineralogist, 103(5), 792–

802. https://doi.org/10.2138/am-2018-6267.

Frank, O., Zukalova, M., Laskova, B., Kürti, J., Koltai, J., and Kavan, L. (2012) Raman spectra of titanium dioxide (anatase, rutile) with identified oxygen isotopes (16, 17, 18). Physical Chemistry Chemical Physics, 14(42), 14567–14572. https://doi.org/10.1039/C2CP42763J.

Gale, A., Dalton, C.A., Langmuir, C.H., Su, Y., and Schilling, J.G. (2013) The mean composition of ocean ridge basalts. Geochemistry, Geophysics, Geosystems, 14, 489–518. https://doi.org/10.1029/2012gc004334

Gerward, L. and Olsen, J.S. (1997) Post-rutile high-pressure phases in TiO_2. Journal of Applied Crystallography, 30(3), 259–264. https://doi.org/10.1107/S0021889896011454.

Gesenhues, U. and Rentschler, T. (1999) Crystal growth and defect structure of Al^{3+}-doped rutile. Journal of Solid State Chemistry, 143(2), 210–218. https://doi.org/10.1006/JSSC.1998.8088.

Gleason, A.E., Jeanloz, R., and Kunz M. (2008) Pressure-temperature stability studies of FeOOH using X-ray diffraction. American Mineralogist, 93, 1882–1885. https://doi.org/10.2138/am.2008.2942.

Guo, H. (2017). In-situ infrared spectra of OH in rutile up to 1000°C. Physics and Chemistry of Minerals, 44(8), 547–552. https://doi.org/10.1007/s00269-017-0881-6.

Haines, J., Leger, J.M., and Chateau, C. (2000) Transition to a crystalline high-pressure phase in α-GeO_2 at room temperature. Physical Review B, 61(13), 8701. https://doi.org/10.1103/PhysRevB.61.8701.

Hazen, R.M. and Finger, L.W. (1981) Bulk moduli and high-pressure crystal structures of rutile-type compounds. Journal of Physics and Chemistry of Solids, 42(3), 143–151. https://doi.org/10.1016/0022-3697(81)90074-3.

Hazen, R.M., Downs, R.T., and Prewitt, C.T. (2000) Principles of comparative crystal chemistry. Reviews in Mineralogy and Geochemistry, 41(1), 1–33. https://doi.org/10.2138/RMG.2000.41.1.

Hirose, K. and Fei, Y. (2002) Subsolidus and melting phase relations of basaltic composition in the uppermost lower mantle. Geochimica et Cosmochimica Acta, 66, 2099–2108. https://doi.org/10.1016/S0016-7037(02)00847-5.

Hirose, K., Takafuji, N., Sata, N., and Ohishi, Y. (2005) Phase transition and density of subducted MORB crust in the lower mantle. Earth and Planetary Science Letters, 237, 239–251. https://doi.org/10.1016/j.epsl.2005.06.035.

Hoff, C.M. and Watson, E.B. (2021) Aluminum solubility in rutile (TiO_2). Physics and Chemistry of Minerals, 48(12), 45. https://doi.org/10.1007/s00269-021-01169-z.

Howard, C.J., Sabine, T.M., and Dickson, F. (1991) Structural and thermal parameters for rutile and anatase. Acta Crystallographica Section B, 47(4), 462–468.

https://doi.org/10.1107/S010876819100335X.

Hwang, S., Shen, P., Chu, H., and Yui, T. (2000) Nanometer-size-PbO_2-type TiO_2 in garnet: A thermobarometer for ultrahigh-pressure metamorphism. Science, 288(5464), 321–324. https://doi.org/10.1126/SCIENCE.288.5464.321.

Irifune, T., Sekine, T., Ringwood, A.E., and Hibberson, W.O. (1986) The ecologite-garnetite transformation at high-pressure and some geophysical implications. Earth and Planetary Science Letters, 77, 245–256. https://doi.org/10.1016/0012-821X(86)90165-2.

Ishii, T., Criniti G., Ohtani, E., Purevjav, N., Fei, H., Katsura, T., and Mao, H.K. (2022) Superhydrous aluminous silica phases as major water hosts in high-temperature lower mantle. Proceedings of the National Academy of Sciences of U.S.A., 119(44), e2211243119. https://doi.org/10.1073/pnas.2211243119.

Johnson, E.A. (2006) Water in nominally anhydrous crustal minerals: speciation, concentration, and geologic significance. Reviews in Mineralogy and Geochemistry, 62(1), 117–154. https://doi.org/10.2138/rmg.2006.62.6

Johnson, O.W., DeFord, J., and Shaner, J.W. (1973) Experimental technique for the precise determination of H and D concentration in rutile (TiO_2). Journal of Applied Physics, 44(7): 3008–3012. https://doi.org/10.1063/1.1662697.

Klotz, S., Chervin, J.C., Munsch, P., and Marchand, G.L. (2009) Hydrostatic limits of 11

pressure transmitting media. Journal of Physics D: Applied Physics, 42, 075413. https://doi.org/10.1088/0022-3727/42/7/075413.

Kudoh, Y. and Takeda, H. (1986) Single crystal X-ray diffraction study on the bond compressibility of fayalite, Fe_2SiO_4 and rutile, TiO_2 under high pressure. Physica, 139–140, 333–336. https://doi.org/10.1016/0378-4363(86)90591-7.

Kuribayashi, T., Sano-Furukawa, A., and Nagase, T. (2014) Observation of pressure-induced phase transition of δ-AlOOH by using single-crystal synchrotron X-ray diffraction method. Physics and Chemistry of Mineral, 41, 303–312. https://doi.org/10.1007/s00269-013-0649-6.

Lan, T., Tang, X., and Fultz, B. (2012) Phonon anharmonicity of rutile TiO_2 studied by Raman spectrometry and molecular dynamics simulations. Physical Review B, 85(9), 094305. https://doi.org/10.1103/PhysRevB.85.094305.

Li, J., Lin, Y., Meier, T., Liu, Z., Yang, W., Mao, H.K., Zhu, S., and Hu, Q. (2023) Silica-water superstructure and one-dimensional superionic conduit in Earth's mantle. Science Advances, 9(35), eadh3784. https://doi.org/10.1126/sciadv.adh3784.

Libowitzky, E. (1999) Correlation of O-H stretching frequencies and O-H…O hydrogen bond lengths in minerals. Monatshefte für Chemie, 130(8), 1047–1059. https://doi.org/10.1007/BF03354882.

Lin, Y., Hu, Q., Meng, Y., Walter, M., and Mao, H.K. (2020) Evidence for the stability of

628 ultrahydrous stishovite in Earth's lower mantle. Proceedings of the National
629 Academy of Sciences of U.S.A., 117(1), 184–189.
630 https://doi.org/10.1073/pnas.1914295117.

631 Lin, Y., Hu, Q., Walter, M. J., Yang, J., Meng, Y., Feng, X., Zhuang, Y., Cohen, R.E. and
632 Mao, H.K. (2022) Hydrous SiO_2 in subducted oceanic crust and H_2O transport to the
633 core-mantle boundary. Earth and Planetary Science Letters, 594, 117708.

634 Linde, R.K. and DeCarli, P.S. (1969) Polymorphic behavior of titania under dynamic
635 loading. The Journal of Chemical Physics, 50(1), 319–325.
636 https://doi.org/10.1016/j.epsl.2022.117708.

637 Litasov, K.D., Kagi, H., Shatskiy, A., Ohtani, E., Lakshtanov, D.L., Bass, J.D., and Ito E.
638 (2007) High hydrogen solubility in Al-rich stishovite and water transport in the
639 lower mantle. Earth and Planetary Science Letters, 262, 620–634.
640 https://doi.org/10.1016/j.epsl.2007.08.015.

641 Litasov, K.D., Ohtani, E., Suzuki, A., Kawazoe, T., and Funakoshi, K. (2004) Absence of
642 density crossover between basalt and peridotite in the cold slabs passing through 660
643 km discontinuity. Geophysical Research Letters, 31.
644 https://doi.org/10.1029/2004GL021306.

645 Lu, X., Gao, S., Wu, P., Zhang, Z., Zhang, L., Li, X., and Qin, X. (2023) In situ
646 high-pressure Raman spectroscopic, single-crystal X-ray diffraction, and FTIR

investigations of rutile and TiO_2II. Minerals, 13, 703. https://doi.org/10.3390/min13050703.

Mao, H.K., Xu, J., and Bell, P.M. (1986) Calibration of the ruby pressure gauge to 800 kbar under quasi-hydrostatic conditions. Journal of Geophysical Research, 91(B5), 4673–4676. https://doi.org/10.1029/jb091ib05p04673.

Maldener, J., Rauch, F., Gavranic, M., and Beran, A. (2001) OH absorption coefficients of rutile and cassiterite deduced from nuclear reaction analysis and FTIR spectroscopy. Mineralogy and Petrology, 71(1–2), 21–29. https://doi.org/10.1007/S007100170043.

Mammone, J.F., Nicol, M., and Sharma, S.K. (1981) Raman spectra of TiO_2-II, TiO_2-III, SnO_2, and GeO_2 at high pressure. Journal of Physics and Chemistry of Solids, 42(5), 379–384. https://doi.org/10.1016/0038-1098(80)91055-8.

McQueen, R.G., Jamieson, J.C., and Marsh, S.P. (1967) Shock-wave compression and X-Ray studies of titanium dioxide. Science, 155(3768), 1401–1404. https://doi.org/10.1126/science.155.3768.1401.

Meagher, E.P. and Lager, G.A. (1979) Polyhedral thermal expansion in the TiO_2 polymorphs; Refinement of the crystal structures of rutile and brookite at high temperature. The Canadian Mineralogist, 17, 77–85.

Meinhold, G. (2010) Rutile and its applications in Earth sciences. Earth-Science Reviews,

102(1–2), 1–28. https://doi.org/10.1016/j.earscirev.2010.06.001.

Murakami, M., Hirose, K., Ono, S., and Ohishi, Y. (2003) Stability of $CaCl_2$-type and α-PbO_2-type SiO_2 at high pressure and temperature determined by in-situ X-ray measurements. Geophysical Research Lettters, 30, 1207. https://doi.org/10.1029/2002GL016722.

Nishihara, Y. and Matsukage, K.N. (2016) Iron-titanium oxyhydroxides as water carriers in the Earth's deep mantle. American Mineralogist, 101(4), 919–927. https://doi.org/10.2138/am-2016-5517.

Nisr, C., Chen, H.W., Leinenweber, K., Chizmeshya, A., Prakapenka, V.B., Prescher, C., Tkachev, S.N., Meng, Y., Liu, Z.X. and Shim, S.H. (2020) Large H_2O solubility in dense silica and its implications for the interiors of water-rich planets. Proceedings of the National Academy of Sciences of U.S.A., 117(18), 9747–9754. https://doi.org/10.1073/pnas.1917448117.

Oganov, A.R., Gillan, M.J., and Price, G.D. (2005) Structural stability of silica at high pressures and temperatures. Physical Review B, 71, 064104. https://doi.org/10.1103/PhysRevB.71.064104.

Olsen, J.S., Gerward, L., and Jiang, J.Z. (1999) On the rutile/α-PbO_2-type phase boundary of TiO_2. Journal of Physics and Chemistry of Solids, 60(2), 229–233. https://doi.org/10.1016/S0022-3697(98)00274-1.

Ono, S. and Mibe, K. (2011) Determination of the phase boundary of the ferroelastic rutile to $CaCl_2$ transition in RuO_2 using in situ high-pressure and high-temperature Raman spectroscopy. Physical Review B, 84(5), 054114. https://doi.org/10.1103/PhysRevB.84.054114.

Paterson, M. (1982) The determination of hydroxyl by infrared absorption in quartz, silicate glasses and similar materials. Bulletin de Mineralogie, 105(1), 20–29. https://doi.org/10.3406/Bulmi.1982.7582.

Pawley, A., McMillan, P.F., and Holloway, J.R. (1993) Hydrogen in stishovite, with implications for mantle water content, Science, 261, 1024–1026. https://doi.org/10.1126/science.261.5124.1024.

Robinson, K., Gibbs, G.V., and Ribbe, P.H. (1971) Quadratic elongation: A quantitative measure of distortion in coordination polyhedra. Science, 172(3983), 567–570. https://doi.org/10.1126/science.172.3983.567.

Rossman, G.R. and Smyth, J.R. (1990) Hydroxyl contents of accessory minerals in mantle eclogites and related rocks. American Mineralogist, 75(7–8), 775–780.

Samara, G.A. and Peercy, P.S. (1973) Pressure and temperature dependence of the static dielectric constants and Raman spectra of TiO_2 (rutile). Physical Review B, 7(3), 1131–1148. https://doi.org/10.1103/PhysRevB.7.1131.

Sato, H., Endo, S., Sugiyama, M., Kikegawa, T., Shimomura, O., and Kusaba, K. (1991)

Baddeleyite-type high-pressure phase of TiO_2. Science, 251(4995), 786–788. https://doi.org/10.1126/science.251.4995.786.

Shannon, R.D. (1976) Revised effective ionic radii and systematic studies of interatomic distances in halides and chalcogenides. Acta Crystallographica Section A, 32, 751–767. https://doi.org/10.1107/S0567739476001551.

Sheldrick, G.M. (2015) Crystal structure refinement with SHELXL. Acta Crystallographica Section C, 71(1), 3–8. https://doi.org/10.1107/S2053229614024218.

Slepetys, R.A. and Vaughan, P.A. (1969) Solid solution of aluminum oxide in rutile titanium dioxide. The Journal of Physical Chemistry, 73(7), 2157–2162. https://doi.org/10.1021/J100727A010.

Sobolev, N.V. and Yefimova, E.S. (2000) Composition and petrogenesis of Ti-oxides associated with diamonds. International Geology Review, 42(8), 758–767. https://doi.org/10.1080/00206810009465110.

Soffer, B.H. (1961) Studies of the optical and infrared absorption spectra of rutile single crystals. Journal of Chemical Physics, 35, 940–945. https://doi.org/10.1063/1.1701242.

Stebbins, J.F. (2007) Aluminum substitution in rutile titanium dioxide: new constraints from high-resolution ^{27}Al NMR. Chemistry of Materials, 19(7), 1862–1869.

https://doi.org/10.1021/CM0629053.

Sugiyama, K. and Takéuchi, Y. (1991) The crystal structure of rutile as a function of temperature up to 1600°C. Zeitschrift für Kristallographie, 194(1–4), 305–314. https://doi.org/10.1524/zkri.1991.194.14.305.

Suito, K., Kawai, N., and Masuda, Y. (1975) High pressure synthesis of orthorhombic SnO_2. Materials Research Bulletin, 10(7), 677–680. https://doi.org/10.1016/0025-5408(75)90050-1.

Swamy, V., Dubrovinskaia, N.A., and Dubrovinsky, L.S. (2002) Compressibility of baddeleyite-type TiO_2 from static compression to 40 GPa. Journal of Alloys and Compounds, 340(1–2), 46–48. https://doi.org/10.1016/S0925-8388(02)00109-3.

Swope, R.J., Smyth, J.R., and Larson, A.C. (1995) H in rutile-type compounds: I. Single-crystal neutron and X-ray diffraction study of H in rutile. American Mineralogist, 80(5–6), 448–453. https://doi.org/10.2138/am-1995-5-605.

Tan, Z., Chen, P., Zhou, Q., Liu, J., Mei, X., Wang, B., and Cui, N. (2018) Shock synthesis and characterization of titanium dioxide with α-PbO_2 structure. Journal of Physics: Condensed Matter, 30(26), 264006. https://doi.org/10.1088/1361-648X/aac709.

Thompson, E.C., Davis, A.H., Brauser, N.M., Liu, Z., Prakapenka, V.B., and Campbell, A.J. (2020) Phase transitions in Ɛ-FeOOH at high pressure and ambient temperature.

American Mineralogist, 105(12), 1769–1777. https://doi.org/10.2138/am-2020-7468.

Tsuchida, Y. and Yagi, T. (1989) A new, post-stishovite high-pressure polymorph of silica. Nature, 340(6230), 217–220. https://doi.org/10.1038/340217A0.

Turcotte, D.R. and Schubert, G. (2002) Geodynamics, 2nd edition, Cambridge University Press. https://doi.org/10.1017/S0016756802217239.

Vlassopoulos, D., Rossman, G.R., and Haggerty, S.E. (1993) Coupled substitution of H and minor elements in rutile and the implications of high OH contents in Nb-and Cr-rich rutile from the upper mantle. American Mineralogist, 78(11–12), 1181–1191.

Wang, S., Su, Y. Wang, Q. Smyth, J.R., Liu, D., Zhu, X., Miao, Y. Hu, Y. and Ye, Y. (2023) Crystal structure, vibrational spectra on trivalent-cation-doped rutile and application in optical materials. The Journal of Physical Chemistry C, 127(25), 12160–12170. https://doi.org/10.1007/s40242-021-1123-5.

Wang, S., Zhang, J., Smyth, J.R., Zhang, J., Liu, D., Zhu, X., Wang, X. and Ye, Y. (2020) Crystal structure, thermal expansivity and high-temperature vibrational spectra on natural hydrous rutile. Journal of Earth Science, 31(6), 1190–1199. https://doi.org/10.1007/s12583-020-1351-5.

White, W.M. and Klein, E.M. (2014) Composition of the oceanic crust. In R.L. Rudnick Ed., Treatise on Geochemistry, The crust, 2nd edition, 4, p. 457–496. Elsevier,

761 Amsterdam. https://doi.org/10.1016/b978-0-08-095975-7.00315-6.

762 Yang, Y., Xia, Q.K., Feng, M., and Gu, X. (2011) In situ FTIR investigations at varying
763 temperatures on hydrous components in rutile. American Mineralogist, 96(11–12),
764 1851–1855. https://doi.org/10.2138/am.2011.3826.

765 Ye, Y., Shim, S.H., Prakapenka, V., and Meng, Y. (2018) Equation of state of solid Ne
766 inter-calibrated with the MgO, Au, Pt, NaCl-B_2, and ruby pressure scales up to 130
767 GPa. High Pressure Research, 38(4), 377–395.
768 https://doi.org/10.1080/08957959.2018.1493477.

769 Zack, T., Kronz, A., Foley, S.F., and Rivers, T. (2002) Trace element abundances in rutiles
770 from eclogites and associated garnet mica schists. Chemical Geology, 184(1–2), 97–
771 122. https://doi.org/10.1016/S0009-2541(01)00357-6.

772 Zhang, Y., Li, L., Liu, Y., Feng, T., Xi, S., Wang, X., Xue, C., Qian, J., and Li, G. (2019)
773 A symbiotic hetero-nanocomposite that stabilizes unprecedented $CaCl_2$-type TiO_2
774 for enhanced solar-driven hydrogen evolution reaction. Chemical Science, 10, 8323–
775 8330. https://doi.org/10.1039/C9SC01216H.

776 Zhou, S., Čižmár, E., Potzger, K., Krause, M., Talut, G., Helm, M., Fassbender, J.,
777 Zvyagin, S.A., Wosnitza, J., and Schmidt, H. (2009) Origin of magnetic moments in
778 defective TiO_2 single crystals. Physical Review B, 79(11), 113201.
779 https://doi.org/10.1103/PhysRevB.79.113201.

Zhu, X., Wang, Z., Ye, Y., Liu, D., Miao, Y., Wang, Q., Hu, Y., and Chen, G. (2023) Equilibrium hydrogen isotope fractionation between portlandite/brucite and water: Implication from the vibrational spectra at elevated temperature and pressure. Chemical Geology, 627, 121470. https://doi.org/10.1016/j.chemgeo.2023.121470.

Figure captions:

Fig. 1. Sketches of **(a)** Rutile-, **(b)** $CaCl_2$- and **(c)** α-PbO_2-type structures viewed in different directions. The larger and smaller (in black) balls represent O^{2-} anion and Ti^{4+} (Al^{3+}) cations, respectively, and the interstitial Al sites are also marked in the $CaCl_2$-type structure as small gray balls.

Fig. 2. (a) Raman and **(b)** mid-FTIR spectra for the synthetic samples in this study, with backgrounds subtracted (hereafter). The thicknesses of the samples have been normalized to 1 cm in **(b)**. The fitted peak positions are labelled in the figures, and some weak bands are magnified for clarity.

Fig. 3. Measured OH stretching wavenumber (in cm^{-1}) *versus* calculated quadratic

799 elongation for incorporated $M^{3+}O_6$ octahedra in various hosts (rutile-TiO_2 phases: Wang
800 et al. 2023; Al-bearing $CaCl_2$-SiO_2: Ishii et al. 2022). The filled and open symbols
801 represent the TiO_2 and SiO_2 hosts, respectively, and the circle, diamond and square
802 shapes stand for the rutile-, $CaCl_2$- and α-PbO_2-type structures, individually. A linear
803 regression (dashed line) is fitted for all the data points.
804
805 **Fig. 4. (a,b,c)** Raman spectra at various temperatures and **(d,e,f)** variation of the
806 vibrational frequencies with temperature for **(a,d)** rutile-$Ti_{0.998}Al_{0.002}O_2$, **(b,e)**
807 $CaCl_2$-$Ti_{0.972}Al_{0.037}O_2$ and **(c,f)** α-PbO_2-$Ti_{0.930}(AlH)_{0.070}O_2$. The phase transitions to
808 rutile-type structure at T = 950 K are marked as vertical dashed lines in (**e,f**). The
809 quenched spectra are shown in gray colors for each sample.
810
811 **Fig. 5. (a,b,c)** High-temperature FTIR spectra and **(d,e,f)** evolution of v_i's with T for the
812 samples of **(a,d)** rutile-$Ti_{0.998}Al_{0.002}O_2$, **(b,e)** $CaCl_2$-$Ti_{0.972}Al_{0.037}O_2$ and **(c,f)**
813 α-PbO_2-$Ti_{0.930}(AlH)_{0.070}O_2$.
814
815 **Fig. 6.** Summary of the T-dependences of **(a)** lattice and **(b)** OH stretching vibrations
816 among the samples in rutile- (open), $CaCl_2$- (gray) and α-PbO_2-type (black) structures.
817

818 **Fig. 7.** Selected high-*P* Raman spectra for **(a)** rutile-$Ti_{0.998}Al_{0.002}O_2$, **(b)**
819 $CaCl_2$-$Ti_{0.972}Al_{0.037}O_2$ and **(c)** α-PbO_2-$Ti_{0.930}(AlH)_{0.070}O_2$, and their fitted vibrational
820 frequencies are plotted as a function of temperature in (**d,e,f**), respectively.

821

822 **Fig. 8.** Representative high-*P* mid-FTIR spectra for **(a)** rutile-$Ti_{0.998}Al_{0.002}O_2$, **(b)**
823 $CaCl_2$-$Ti_{0.972}Al_{0.037}O_2$ and **(c)** α-PbO_2-$Ti_{0.930}(AlH)_{0.070}O_2$, and variation of the OH
824 stretching frequencies with temperature are illustrated in (**d,e,f**), individually.

825

826 **Fig. 9**. Comparison for the *P*-dependences of the **(a)** lattice and **(b)** OH stretching modes
827 among the TiO_2 polymorphs involved in this study.

828

This is the peer-reviewed, final accepted version for American Mineralogist, published by the Mineralogical Society of America.
The published version is subject to change. Cite as Authors (Year) Title. American Mineralogist, in press.
DOI: https://doi.org/10.2138/am-2024-9316. http://www.minsocam.org/

Table 1. Synthesis conditions of the samples and the calibrated Al^{3+} and H^{+} concentrations with statistical uncertainties.

	Starting Materials (wt. %)	*P* (GPa)	*T* (K)	Al/10^6 Ti	H/10^6 Ti[a]	H/10^6 Ti[b]	H/10^6 Ti[c]
Rutile-type	TiO_2 (95) + Al_2O_3 (5)	0	1873	2265±309	421±190	335±160	1938±893
$CaCl_2$-type	TiO_2 (95) + Al_2O_3 (5) + 1μL H_2O	7	1373	54761±828	603±267	479±215	3820±1647
	TiO_2 (93) + $Al(OH)_3$ (7) + 1μL H_2O	7	1373	37893±2048	3695±1450	2937±1152	9728±4562
α-PbO_2-type	TiO_2 + 1μL H_2O	14	1673	--	--	--	--
	TiO_2 (95) + Al_2O_3 (5) + 1μL H_2O	14	1673	44695±6236	47987±18760	38137±14910	53913±19456

This is the peer-reviewed, final accepted version for American Mineralogist, published by the Mineralogical Society of America.
The published version is subject to change. Cite as Authors (Year) Title. American Mineralogist, in press.
DOI: https://doi.org/10.2138/am-2024-9316. http://www.minsocam.org/

TiO_2 (93) + $Al(OH)_3$ (7) + 1μL H_2O	14	1673	74670±6493	84029±26895	66781±21374	71706±16043

There calibrations are adopted for determining the water concentrations in the products: ***a***: Johnson et al (1973); ***b***: Maldener et al (2001); ***c***: Paterson (1982).

829

Table 2. The unit-cell and intensity collection parameters for the synthetic TiO_2 samples with various Al^{3+} concentrations.

	Rutile-type	$CaCl_2$-type			α-PbO_2-type	
	$Ti_{0.998}Al_{0.002}O_2$	$Ti_{0.961}Al_{0.053}O_2$	$Ti_{0.972}Al_{0.037}O_2$	TiO_2	$Ti_{0.957}(AlH)_{0.043}O_2$	$Ti_{0.930}(AlH)_{0.070}O_2$
a (Å)	4.5957(6)	4.5963(3)	4.5930(3)	4.5314(3)	4.5169(2)	4.5184(15)
b (Å)	4.5957(6)	4.5856(3)	4.5902(3)	5.4983(5)	5.5021(3)	5.5101(14)
c (Å)	2.9591(8)	2.9524(2)	2.9553(2)	4.9001(4)	4.9024(3)	4.9135(15)
V (Å^3)	62.50(2)	62.227(7)	62.306(7)	122.086(17)	121.837(11)	122.33(6)
ρ_{calc} (g/cm^3)	4.246(1)	4.241(4)	4.233(4)	4.347(8)	4.307(6)	4.259(3)
N_{total}	1940	2048	1837	3334	2568	2960
N_{unique}	173	435	206	454	360	451
R_1 for all refl.	0.0403	0.0405	0.0282	0.0447	0.0300	0.0369

R_1 for $I > 2\sigma$	0.0343	0.0361	0.0262	0.0345	0.0273	0.0319
R_{int}	0.0786	0.0423	0.0438	0.0614	0.0373	0.0454
GooF	1.010	1.062	1.185	1.093	1.118	1.1067

831

Table 3. Atomic occupancies and coordinates for the synthetic samples from the single-crystal structure refinements.

			Rutile-type	$CaCl_2$-type		α-PbO_2-type		
			$Ti_{0.998}Al_{0.002}O_2$	$Ti_{0.961}Al_{0.053}O_2$	$Ti_{0.972}Al_{0.037}O_2$	TiO_2	$Ti_{0.957}(AlH)_{0.043}O_2$	$Ti_{0.930}(AlH)_{0.070}O_2$
Occupancies*	Ti		0.998	0.961	0.972	1	0.957	0.930
	Al^{oct}		0.002	0.039	0.028	0	0.043	0.070
	Al^{int} $		--	0.007	0.0045	--	--	--
Atomic	O	*x*	0.3048(3)	0.3035(2)	0.3049(2)	0.2700(2)	0.2695(2)	0.2687(2)
Coordinate		*y*	0.3048(3)	0.3061(2)	0.3042(3)	0.3820(2)	0.3822(1)	0.3823(1)

This is the peer-reviewed, final accepted version for American Mineralogist, published by the Mineralogical Society of America.
The published version is subject to change. Cite as Authors (Year) Title. American Mineralogist, in press.
DOI: https://doi.org/10.2138/am-2024-9316. http://www.minsocam.org/

	z	0#	0#	0#	0.4182(3)	0.4187(2)	0.4188(2)
Ti/Al^{oct}	*x*	0#	0#	0#	0#	0#	0#
	y	0#	0#	0#	0.1722(2)	0.1712(5)	0.1708(5)
	z	0#	0#	0#	0.25#	0.25#	0.25#

832 *: the occupancies are calculated based on the EPMA measurements; #: the atomic coordinates are fixed during the structure

833 refinements. **$**: Al^{int} site are fixed at (0.2, 0.5, 0) in the $CaCl_2$-type structure.

834

Table 4. Calculated Ti(Al)-O bond length and O-O edges for the Ti(Al)O_6 octahedra.

Sample	rutile-type	$CaCl_2$-type		α-PbO_2 -type		
	$Ti_{0.998}Al_{0.002}O_2$	$Ti_{0.961}Al_{0.053}O_2$	$Ti_{0.972}Al_{0.037}O_2$	TiO_2	$Ti_{0.957}(AlH)_{0.043}O_2$	$Ti_{0.930}(AlH)_{0.070}O_2$
Ti(Al)-O (Å)	1.9490(10) ×4	1.9456(6) ×4	1.9479(8) ×4	1.8726(11) ×2	1.8745(8) ×2	1.8761(8) ×2
	1.9810(17) ×2	1.9790(9) ×2	1.9776(12) ×2	1.9541(13) ×2	1.9518(8) ×2	1.9561(9) ×2

	--	--	--	2.0765(12) ×2	2.0724(8) ×2	2.0755(8) ×2
O-O (Å)	2.5373(20) ×2	2.5346(12) ×2	2.5383(17) ×2	2.5829(15) ×1	2.5795(10)×1	2.5864(12) ×1
	2.7790(17) ×8	2.7709(10) ×4	2.7758(12) ×4	2.6575(17) ×1	2.6593(11) ×1	2.6681(13) ×1
	2.9591(8) ×2	2.7795(10) ×4	2.7758(17) ×4	2.7551(16) ×2	2.7567(10) ×2	2.7602(12) ×2
	--	2.9524(2) ×2	2.9553(2) ×2	2.7725(20) ×2	2.7727(12) ×2	2.7784(13) ×2
	--	--	--	2.8077(14) ×2	2.8025(10) ×2	2.8045(12) ×2
	--	--	--	2.8535(20) ×2	2.8560(11) ×2	2.8615(13) ×2
	--	--	--	2.8834(14) ×1	2.8707(10) ×1	2.8667(13) ×1
	--	--	--	2.9504(16) ×1	2.9423(10) ×1	2.9404(13) ×1
Octa. V (Å^3)	9.916(11)	9.873(7)	9.887(9)	9.900(12)	9.887(9)	9.937(9)

835

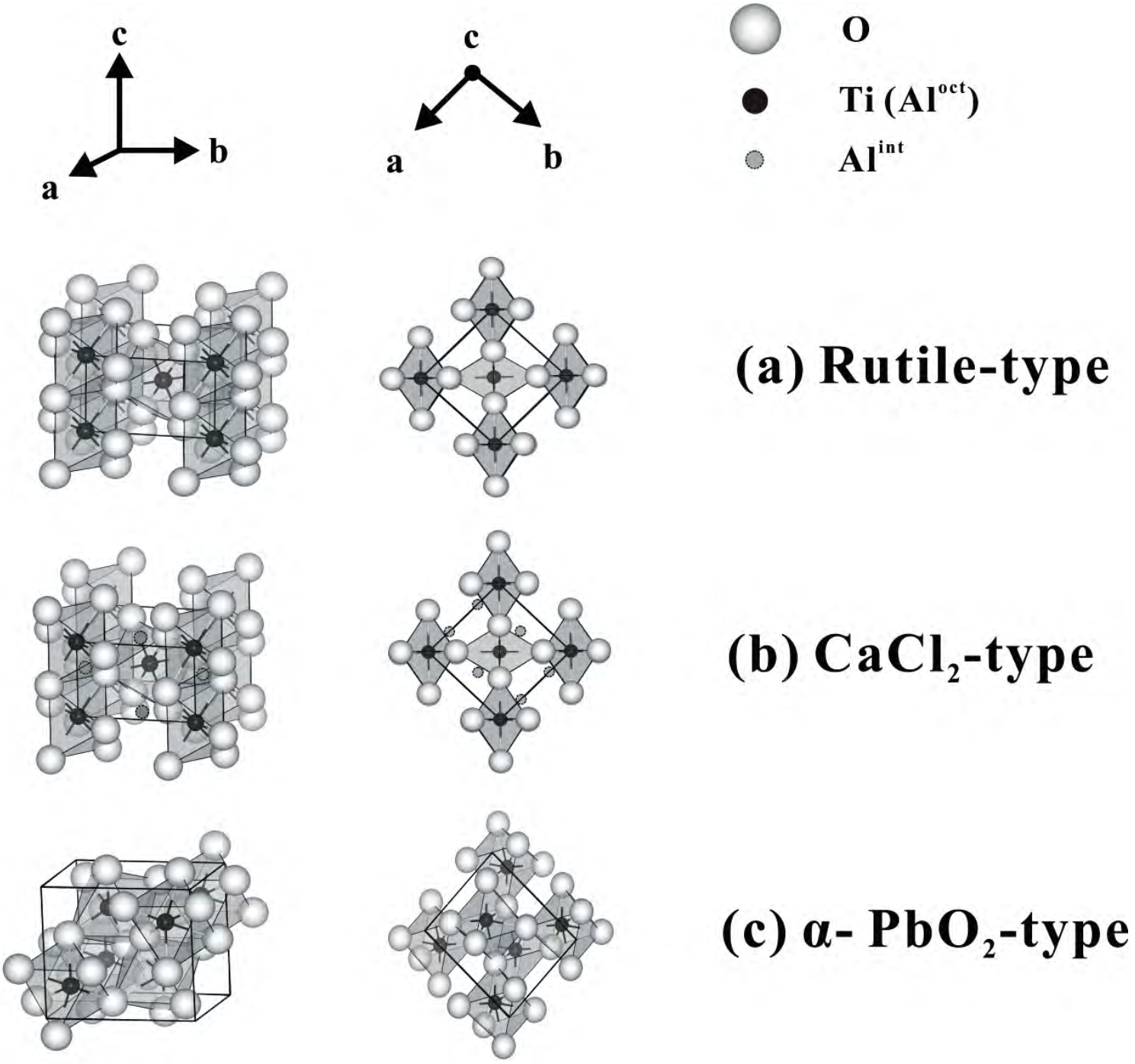

Figure 1

This is the peer-reviewed, final accepted version for American Mineralogist, published by the Mineralogical Society of America.
The published version is subject to change. Cite as Authors (Year) Title. American Mineralogist, in press.
DOI: https://doi.org/10.2138/am-2024-9316. http://www.minsocam.org/

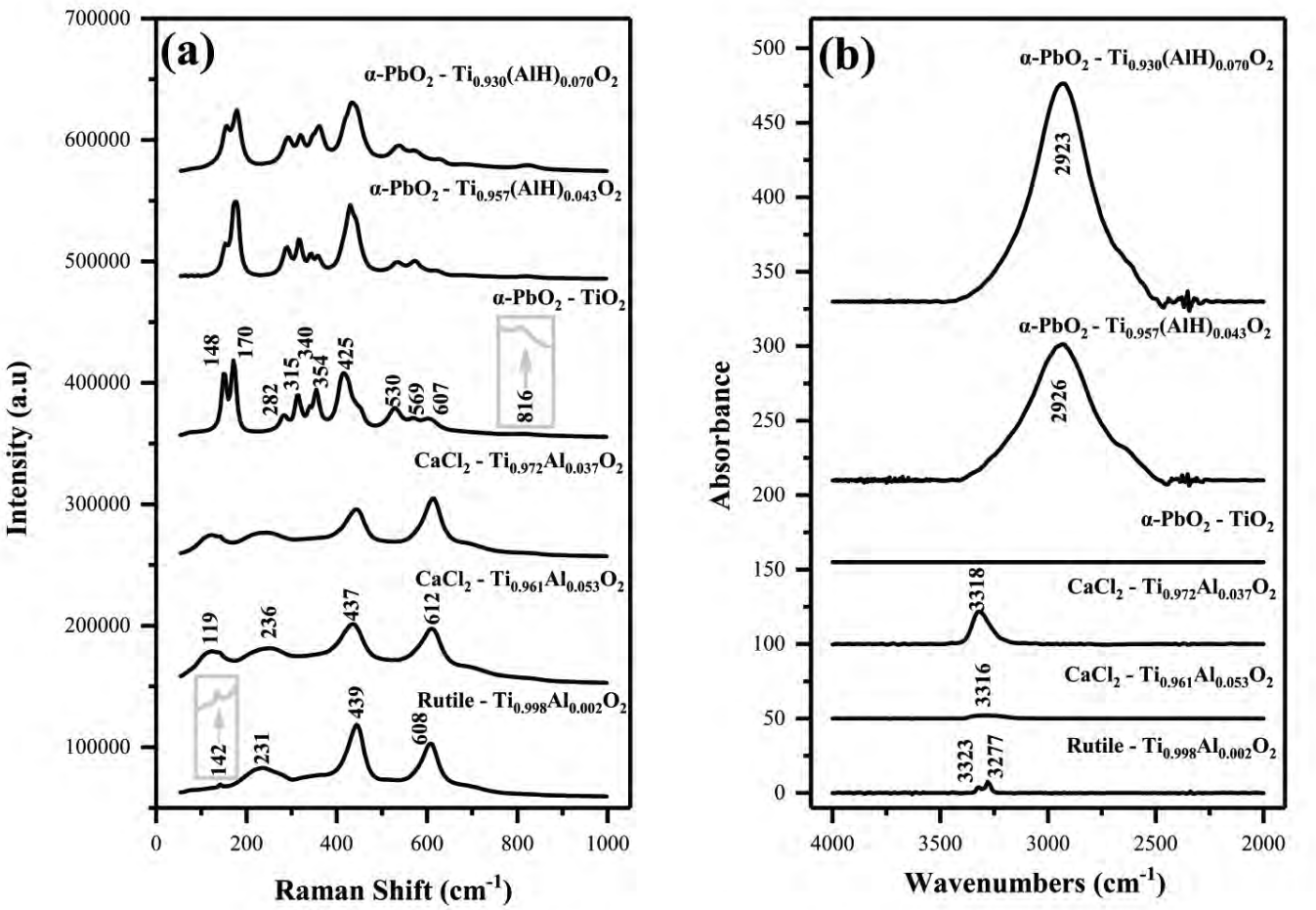

Figure 2

This is the peer-reviewed, final accepted version for American Mineralogist, published by the Mineralogical Society of America.
The published version is subject to change. Cite as Authors (Year) Title. American Mineralogist, in press.
DOI: https://doi.org/10.2138/am-2024-9316. http://www.minsocam.org/

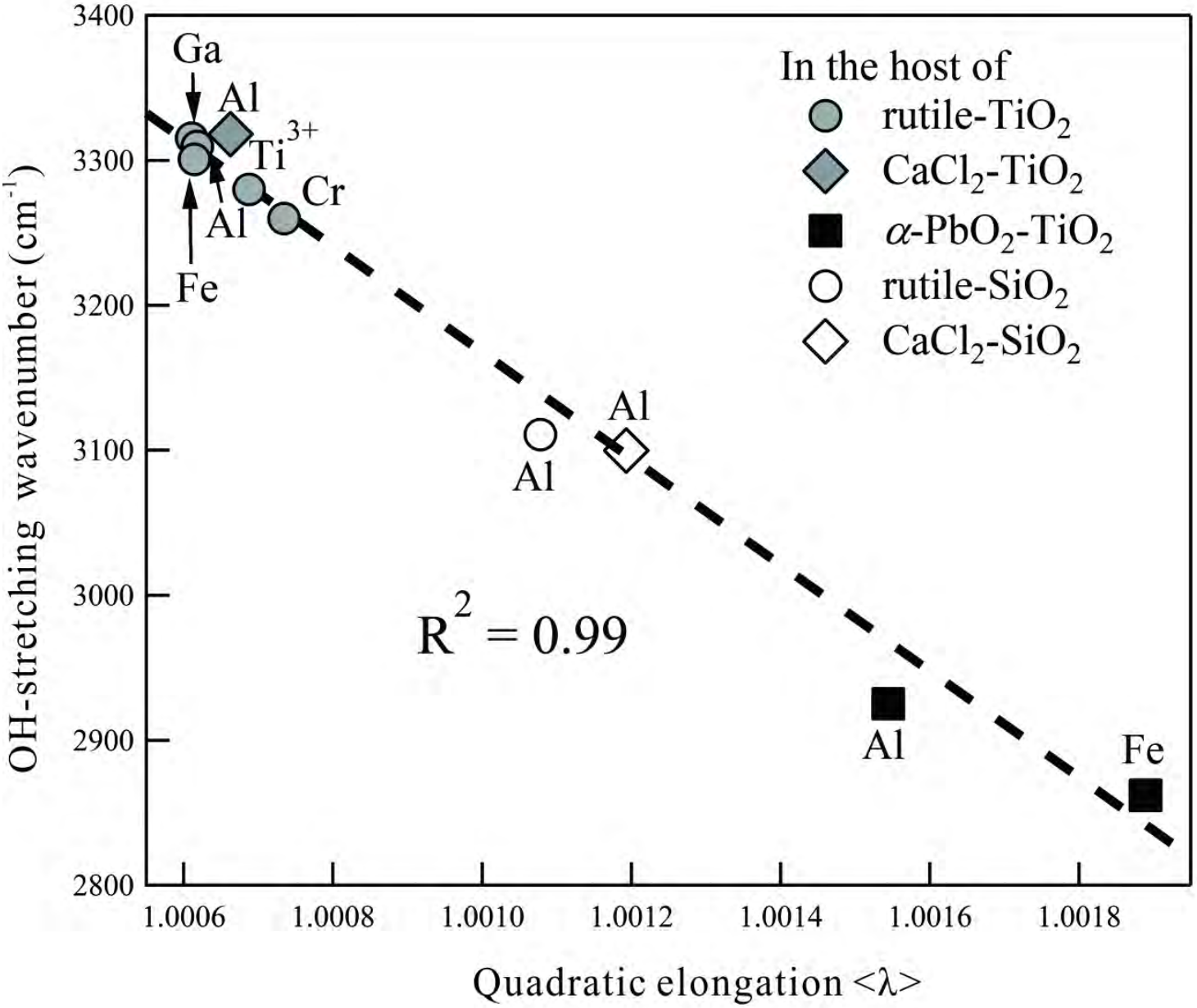

Figure 3

This is the peer-reviewed, final accepted version for American Mineralogist, published by the Mineralogical Society of America.
The published version is subject to change. Cite as Authors (Year) Title. American Mineralogist, in press.
DOI: https://doi.org/10.2138/am-2024-9316. http://www.minsocam.org/

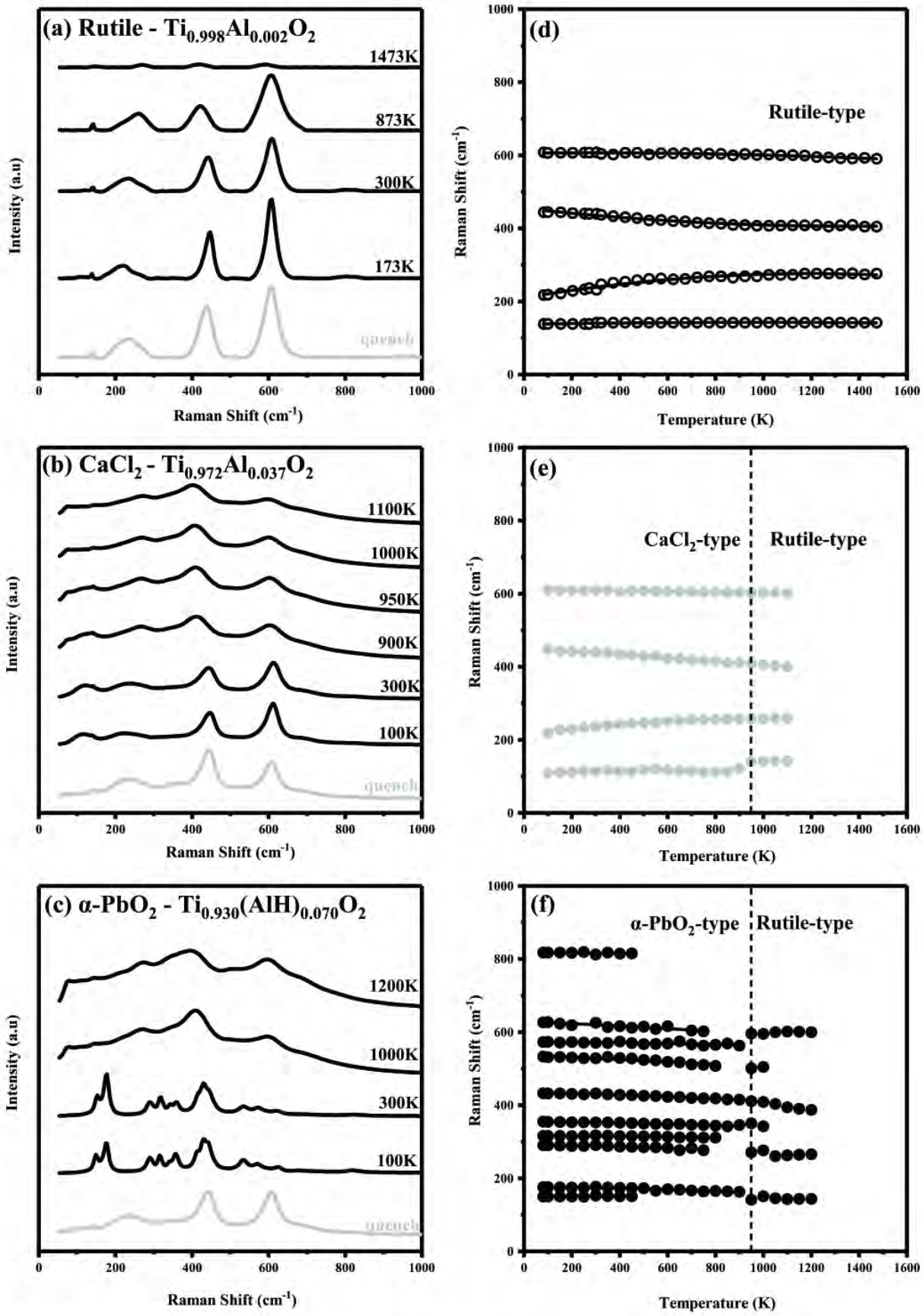

Figure 4

This is the peer-reviewed, final accepted version for American Mineralogist, published by the Mineralogical Society of America.
The published version is subject to change. Cite as Authors (Year) Title. American Mineralogist, in press.
DOI: https://doi.org/10.2138/am-2024-9316. http://www.minsocam.org/

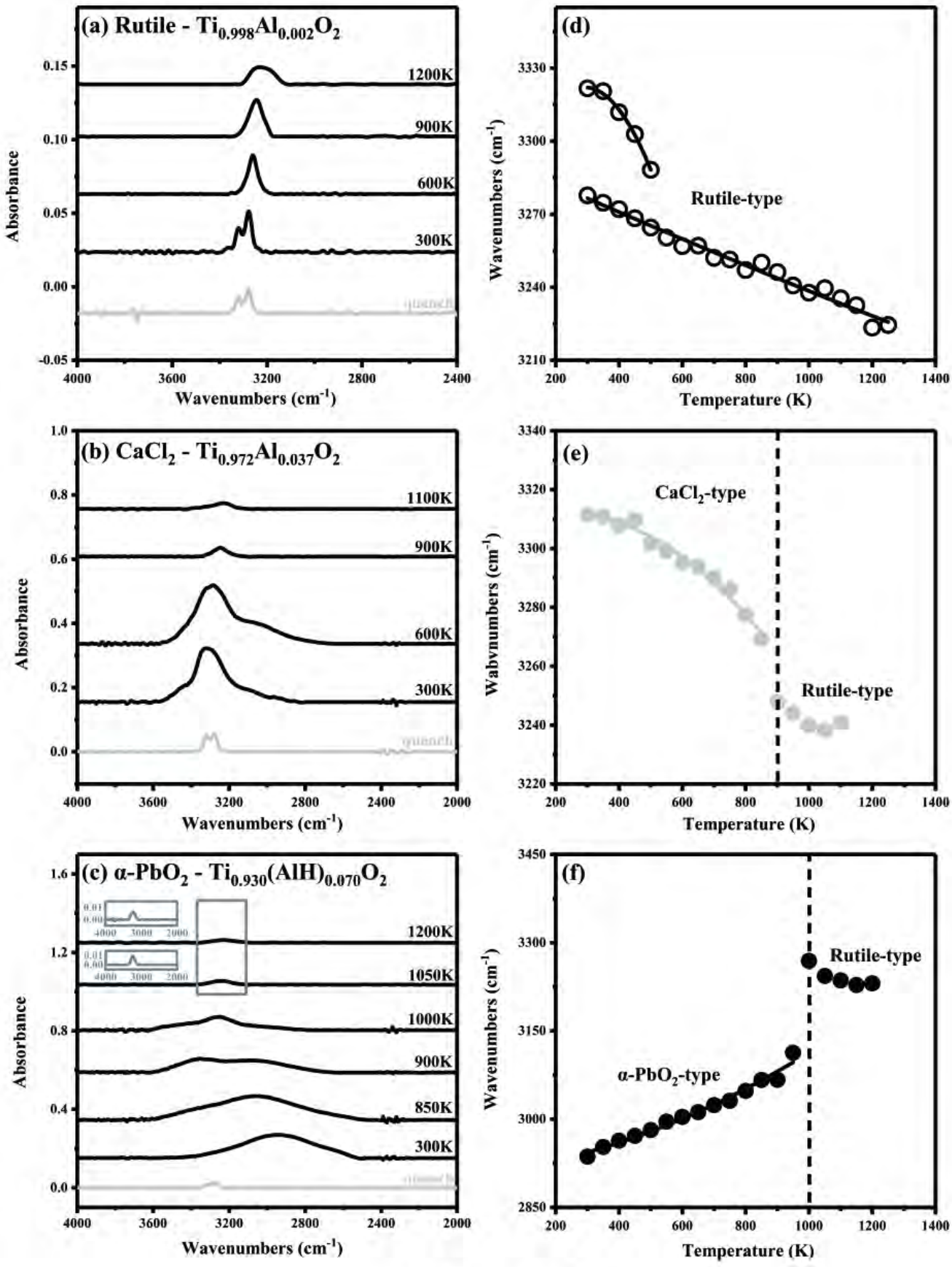

Figure 5

This is the peer-reviewed, final accepted version for American Mineralogist, published by the Mineralogical Society of America.
The published version is subject to change. Cite as Authors (Year) Title. American Mineralogist, in press.
DOI: https://doi.org/10.2138/am-2024-9316. http://www.minsocam.org/

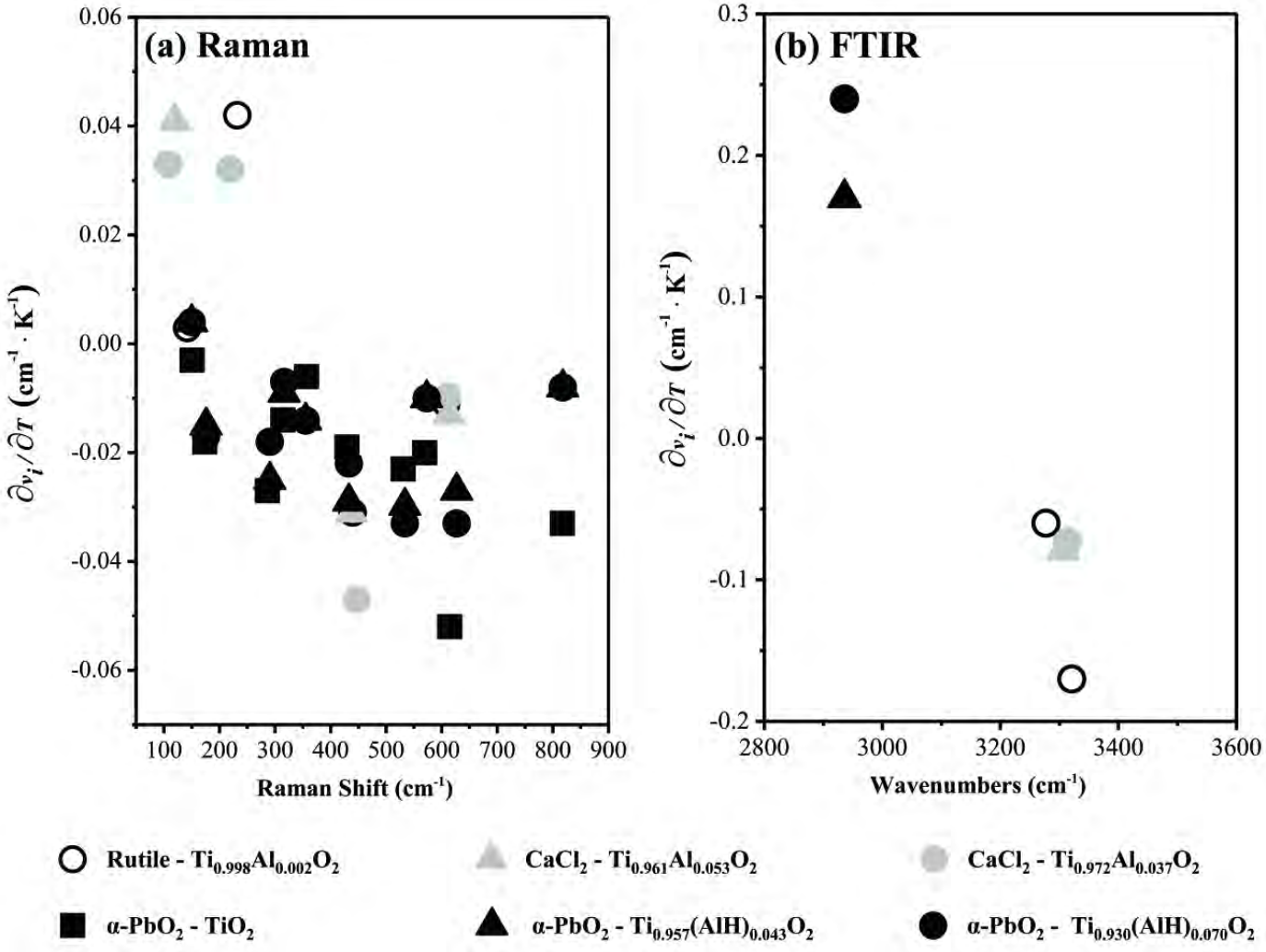

Figure 6

This is the peer-reviewed, final accepted version for American Mineralogist, published by the Mineralogical Society of America.
The published version is subject to change. Cite as Authors (Year) Title. American Mineralogist, in press.
DOI: https://doi.org/10.2138/am-2024-9316. http://www.minsocam.org/

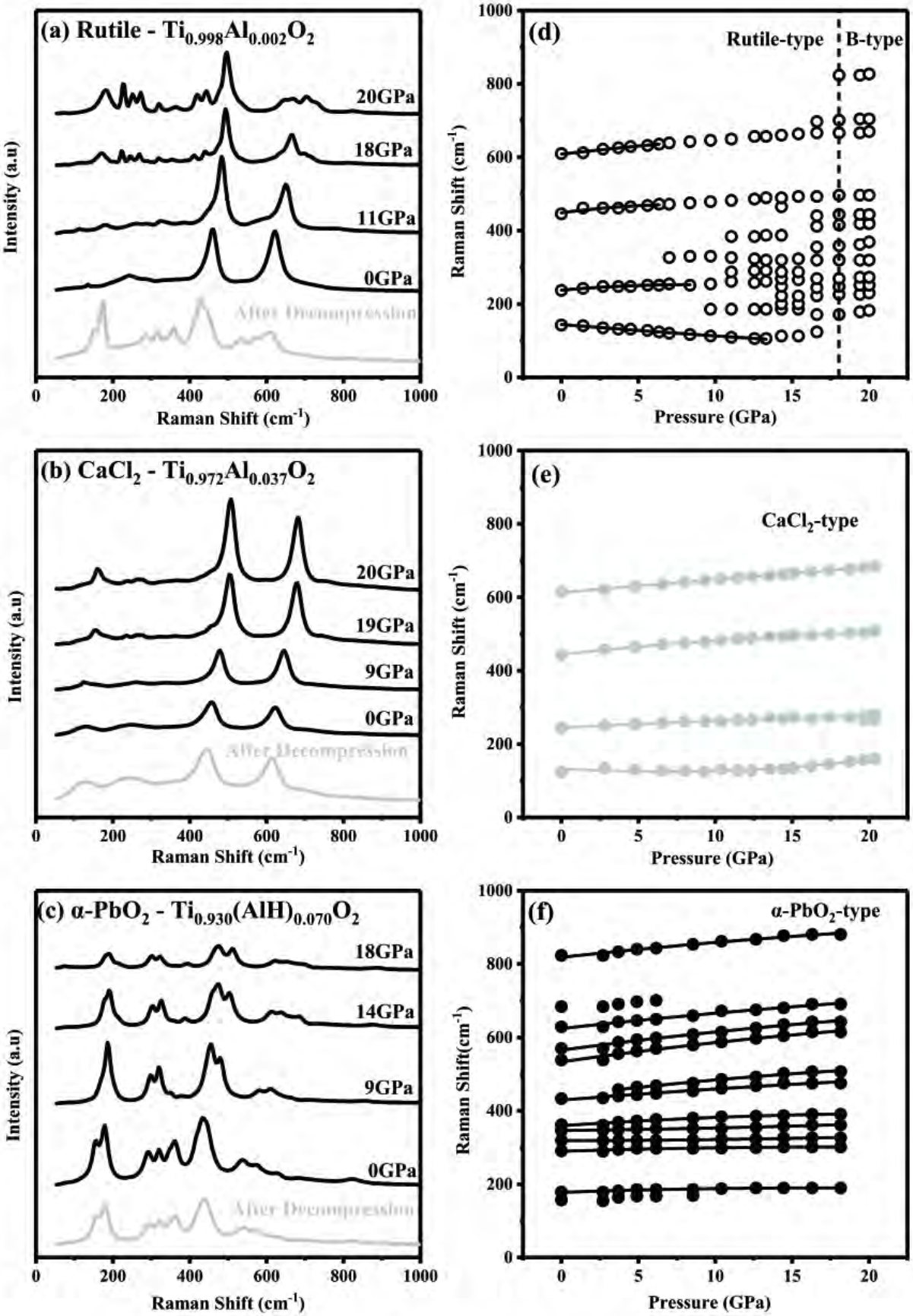

Figure 7

This is the peer-reviewed, final accepted version for American Mineralogist, published by the Mineralogical Society of America.
The published version is subject to change. Cite as Authors (Year) Title. American Mineralogist, in press.
DOI: https://doi.org/10.2138/am-2024-9316. http://www.minsocam.org/

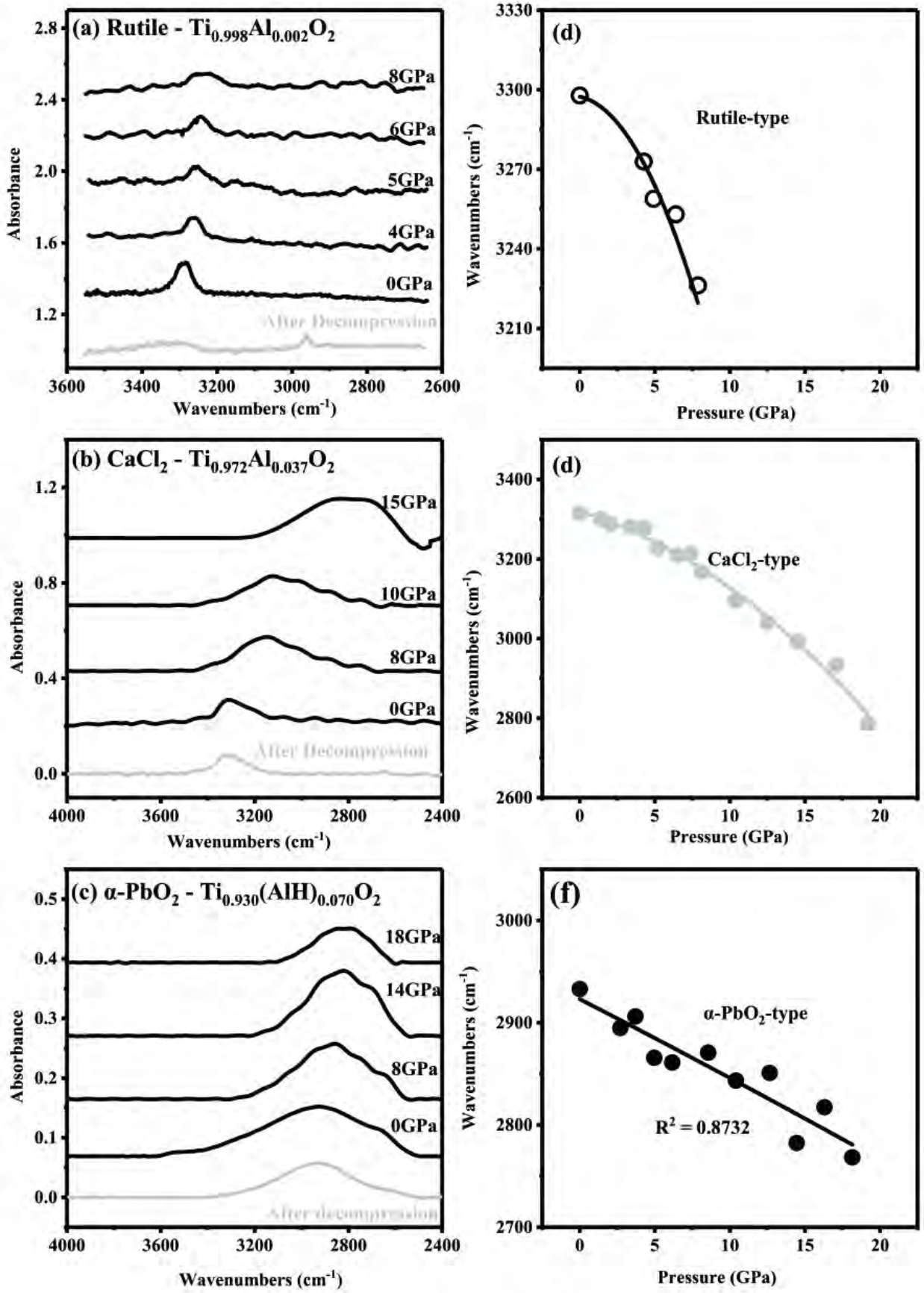

Figure 8

This is the peer-reviewed, final accepted version for American Mineralogist, published by the Mineralogical Society of America.
The published version is subject to change. Cite as Authors (Year) Title. American Mineralogist, in press.
DOI: https://doi.org/10.2138/am-2024-9316. http://www.minsocam.org/

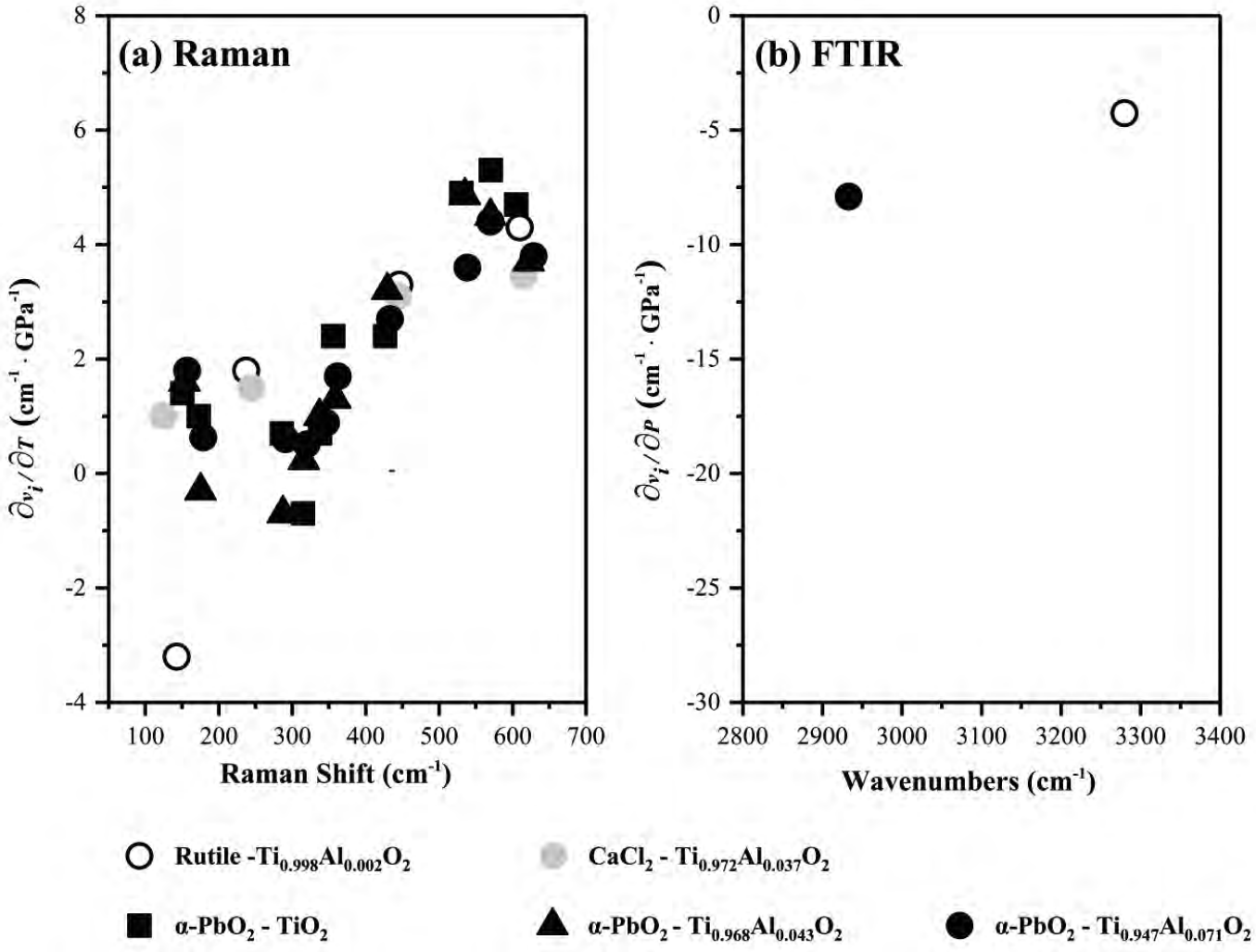

Figure 9